

Ratchetting and creep failure in twin-wall turbine blades experiencing severe thermal and centrifugal loading

Christos G. Skamniotis and Alan C.F. Cocks

Department of Engineering Science, University of Oxford, Parks Road,
Oxford OX7 6DP, UK

ABSTRACT

Twin-wall structures can be cooled both externally and internally, raising great potential for use in high temperature applications. However, their increased geometric complexity imposes a range of potential failure mechanisms for consideration in design. The primary aim of this study is to identify the nature of such mechanisms by constructing Bree type interaction diagrams for idealised double wall systems under cyclic thermomechanical loading which show the combination of loading conditions for which cyclic plasticity (leading to fatigue failure)-creep-ratchetting occur. Through an extension of the classical Bree analysis we determine analytical boundaries between different regimes of behaviour. We also quantify the effects of wall thickness ratio, temperature field as well as yield and creep material properties. Local cyclic plasticity is shown to dominate over structural/global ratchetting when the yield strength reduces with temperature and/or when the temperature gradient through the hot wall thickness dominates over the temperature difference between the walls. Thus, we conclude that global ratchetting is unlikely to occur in the practical loading range of Nickel based twin-wall turbine blades, but instead these systems suffer from local fatigue at cooling holes and excessive creep deformation. This is verified by 3D cyclic Finite Element (FE) simulations, demonstrating that the analytical approach provides a powerful, cost-effective strategy for: providing physical insight into possible deformation mechanisms in a range of thin-walled components; highlighting the key trade-offs to be considered in design; and directing the use of computer methods towards more detailed calculations.

Keywords: thermomechanical loading, shakedown, ratchetting, creep, double wall transpiration cooled turbine blade.

Nomenclature

Abbreviations

DWTC = double wall transpiration cooling

TM = thermomechanical

FE = Finite elements

2D = two-dimensional

3D = three-dimensional

SCF = stress concentration factor

Symbols

Thermal

T_{max} = maximum temperature in the structure / temperature at the outer hot wall surface (°C)

T_{med} = temperature at the inner hot wall surface (°C)

T_{min} = minimum temperature in the structure / cool wall temperature (°C)

T_0 = room temperature (°C)

T_o = reference temperature for creep law (°C)

ΔT = global temperature difference in the system (°C)

ΔT_h = temperature difference across the hot wall thickness (°C)

$\bar{\Delta T}_h$ = temperature difference across the hot wall thickness normalised by the global temperature difference in the system

$T_h(y)$ = temperature as a function of through thickness position in the hot wall (°C)

\bar{T}_h = average hot wall temperature (°C)

T_{tr} = transition temperature between the cold and hot yield stress regimes (°C)

Structural

t_h = hot wall thickness (mm)

t_c = cool wall thickness (mm)

\bar{t}_h = hot wall thickness normalised by total structural thickness

\bar{t}_c = cool wall thickness normalised by total structural thickness

R = geometric radius of curvature (mm)

H = pedestal height (mm)

S = total wall cross sectional area (mm)

D_{film} = film hole diameter (mm)

D_{imp} = impingement hole diameter (mm)

y = through thickness position in the hot wall (mm)

ξ = local through thickness position in the hot wall (mm)

y_{tr} = transition position between hot and cold yield strength regions in the hot wall (mm)

a = distance of lower elastic-plastic interface from the middle hot wall axis (mm)

b = distance of upper elastic-plastic interface from the middle hot wall axis (mm)

Material

E = Young's Modulus (MPa)

ν = Poisson's ratio

α = thermal expansion coefficient (m/m·K)

Q = activation energy (KJ/mol)

R = universal gas constant (J/mol·K)

$\dot{\epsilon}_o$ = reference creep rate (1/h)

σ_o = reference stress for creep law (MPa)

n = creep power law exponent

σ_y = (constant) yield stress (MPa)

σ_{y_T} = temperature dependent yield stress (MPa)

$\sigma_{y_h}(y)$ = temperature dependent yield stress as a function of through thickness position in the hot wall (MPa)

σ_{y_c} = temperature dependent yield stress in the cool wall (MPa)

σ_{y_0} = yield stress at room temperature (MPa)

$\bar{\sigma}_y$ = average yield stress (MPa)

Mechanical

$p(\tau)$ = instantaneous mechanical stress/pressure at an instance, τ , in the cycle (MPa)

$\sigma_T(\tau)$ = scaling factor for the instantaneous thermoelastic stress amplitude at an instance, τ , in the cycle (MPa)

p = maximum mechanical stress/pressure occurring in the steady state region of the cycle (MPa)

p_{net} = augmented maximum mechanical stress/pressure in the steady state region of the cycle (MPa)

σ_T = maximum thermoelastic stress occurring in the steady state region of the cycle (MPa)

p^s = maximum mechanical stress/pressure at a shakedown (SR or PR) boundary (MPa)

σ_T^s = maximum thermoelastic stress amplitude at a shakedown (SR or PR) boundary (MPa)

$\hat{\sigma}_h(y, \tau)$ = instantaneous elastic stress in hot wall (MPa)

$\hat{\sigma}_c(\tau)$ = instantaneous elastic stress in cool wall (MPa)

$\hat{\sigma}_h^s(y, \tau)$ = instantaneous elastic stress in hot wall at a shakedown (SR or PR) boundary (MPa)

$\hat{\sigma}_c^s(\tau)$ = instantaneous elastic stress in cool wall at a shakedown (SR or PR) boundary (MPa)

$\sigma_h(y, \tau)$ = instantaneous stress in hot wall (MPa)

$\sigma_c(\tau)$ = instantaneous stress in cool wall (MPa)

$\varepsilon_{p_h}(y, \tau)$ = instantaneous plastic strain in hot wall

$\varepsilon_{p_c}(\tau)$ = instantaneous plastic strain in cool wall

$\Delta\sigma_{h_{cr}}$ = amount of stress relaxation at the location of maximum temperature (MPa)

p^{CR} = maximum mechanical stress/pressure at creep-ratchetting failure (CR) line (MPa)

p^C = maximum mechanical stress/pressure at global creep failure (C) line (MPa)

$\dot{\varepsilon}_{cr}$ = creep strain rate (1/h)

Z = elastic follow-up factor

Time

τ = time instance

t_{dwell} = steady state temperature/creep dwell time period (h)

k = temperature/load scaling factor corresponding to time instance τ_k

Failure

$N_{1\%}$ = cycles required for total creep strain accumulation of 1%, i.e. $\varepsilon_{cr_{1\%}} = 0.01$

1. Introduction

Research on double wall transpiration cooling (DWTC) has been increasingly active over the last five years, as it promises remarkable gains in gas turbine efficiency [1]. These benefits are realised by increasing the gas turbine inlet temperature beyond current levels. The implementation of DWTC in high pressure turbine blade components (see Fig 1a), however, results in them experiencing extreme thermomechanical (TM) loading [2-4], which can be a barrier to the widespread adoption of this technology in practice.

Studies on aerothermal and mechanical aspects of DWTC currently consist of a short list of recent reports [1-3, 5-14]. On the aerothermal side, cooling arises from a combination of processes: (a) impingement cooling internally via flow through impingement holes in the internal cool wall; (b) film cooling due to directed flow through angled film holes in the external hot wall; and (c) conductive cooling along pedestals connecting the walls (see Fig 1b). On the mechanical side, it has been highlighted that cyclic plasticity (which can result in low cycle fatigue failure) in the vicinity of film holes is critical [2], due to severe stress concentration effects accompanied by severe thermomechanical (TM) stresses arising from kinematic constraints, temperature variations within the structure, as well as centrifugal loading [15]. Plasticity is also enhanced by the reduction of yield strength of Ni-superalloys used in the blade manufacture at high temperatures [2].

Non-local failure modes, on the other hand, such as structural ratchetting (incremental plastic collapse) and global creep failure, were suggested to be less critical in a preceding paper by the authors [16]. This is because the current in-service TM loading range in turbine blades was found to lie within the shakedown regime. The analysis, however, assumed a 2D two-bar structure without holes and thermal loading was manifested only by a temperature difference between the walls. In practise, the presence of cooling holes, the three dimensions of the structure and the temperature gradient through the outer wall thickness (detailed in [3]) complicate the overall shakedown analysis by allowing more complex ratchet mechanisms to occur, which can alter the above conclusions.

For this reason, in this study we extend substantially our 2D analytical framework to fully capture the influence of temperature gradient on various ratchet and creep boundaries and then validate the calculations through detailed 3D FE simulations. We analyse theoretically the idealised 2D problem shown in Figs 1c-d, where the temperature field is described by three parameters: the maximum temperature, T_{max} , the total temperature difference in the system, $\Delta T = T_{max} - T_{min}$, and the ratio of temperature difference across the hot wall compared to the total temperature difference, $\overline{\Delta T}_h = \Delta T_h / \Delta T$ (see Figs 1c-d). The latter is expected to induce non-linearity in the interaction diagram because the plastically deformed volume in the hot wall will vary for different thermal and mechanical stress amplitudes, as for example seen in the Bree plate [17]. It will be shown later that this aspect combined with the coupling of the two walls gives rise to forms of ratchet mechanisms not previously reported in Bree type problems, let alone in two bar/wall structures. A novel characteristic is that plasticity may not always occur at the two extremes of the loading cycle, and as a result, careful treatment is required when determining the shakedown boundary to determine the precise instants in the cycle that plastic deformation occurs within the system of governing kinematic and equilibrium equations.

The objective of this paper is to provide an overview of the different types of structural response that can occur in practice under the full range of thermomechanical loading conditions that can occur in practice. To facilitate this, we adopt a simple isotropic elastic-perfectly plastic-creep material model with temperature dependent yield strength that captures the major trends in material behaviour. This allows us develop analytical models that allows us to evaluate and understand the interactions between different types of behaviour. Certain types of material behaviour, such as material ratchetting, associated with microstructural phenomena typically observed in polycrystalline metals are not captured by these models [18, 19]. Our focus is on understanding the structural/global ratchetting mechanisms, which are known to induce considerable complexity in the structural behaviour [16] even for relatively simple descriptions of material behaviour. The objective here is to map out when cyclic plastic deformation (leading to fatigue failure), ratchetting and excessive creep deformation dominate the structural response. These types of response can arise in any material and structure that undergoes cyclic thermomechanical loading whereas material ratchetting is material specific and depends on microstructural aspects and the local cyclic stress state [18, 20, 21]. For example, in the single crystal Ni alloys of interest here material ratchetting has been shown to occur under cyclic loading around a non-zero mean stress [22, 23], implying that the effect may be practically inevitable and cannot be avoided through design. On the other hand, as it will be shown here, global ratchetting mechanisms can be avoided if the effects of various design parameters on the ratchet limit is known, e.g. the wall thickness ratio, the scale and the form of the temperature field,

the severity of centrifugal loading as well as the material yield and creep properties. Thus, our objective here is to determine the effects of these geometric and general material properties and develop conservative, straightforward and compact analytical relationships that can be used to identify when global ratchetting is unlikely to occur, rather than to calculate ratchet rates and creep-fatigue life. This information can then aid the development of routine design and assessment procedures that often require quick order-of-magnitude estimations. Note, however, that material ratchetting will influence the global ratchetting mechanisms studied here and it is practically impossible to separate out the two effects; the interplay of these two effects will be explored in future studies. The analytical models also help in directing the use of more detailed calculations for specific sets of load-geometry conditions, as well as in interpreting results from these detailed analyses (which are often numerical). They also provide a framework for interpreting simulations using more elaborate material models, such as those developed to model material ratchetting. It is further noted that the analytical route employed here offers physical insights that are difficult to gain through direct/numerical methods and does not rely on assumptions for the determination of reverse plasticity-ratchet (PR) boundaries, as for example the assumption of constant ratchet strain along the PR boundary, currently used by direct methods [24, 25].

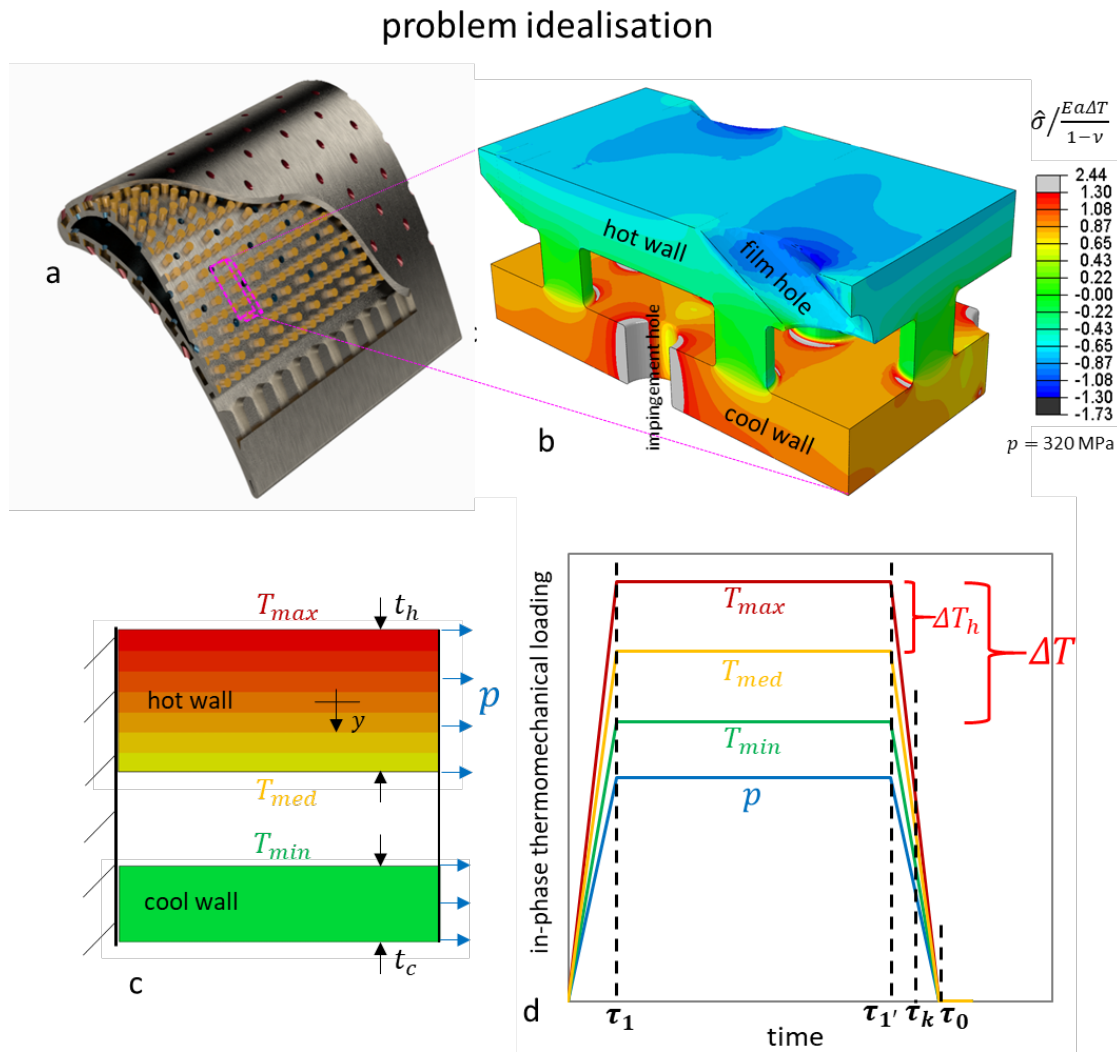


Figure 1. (a) DWTC turbine blade model - adapted from [1]. (b) Elastic stress field arising from TM loading in a unit block representative of Fig 1a - reproduced from [3]. (c) 2D plane stress double wall idealisation of the problem in Fig 1b, featuring a typical steady state temperature field along with the uniform steady state pressure, p (mechanical loading). (d) In-phase TM loading cycle considered throughout this study, with $\Delta T = T_{max} - T_{min}$ and $\Delta T_h = T_{max} - T_{med}$.

2. Problem set-up

This section provides the theoretical basis and essential information for the preliminary calculations and considerations in Section 3 and the construction of interaction diagrams in Section 4. Fig 1a shows a typical double walled high pressure turbine blade. A unit cell taken from a region of low curvature is shown in Fig 1b, which shows the two walls joined by pedestals, effusion holes through the inner wall and film holes in the outer wall. Detailed thermal analyses reveals that in flight there is a linear variation of temperature through the outer wall, while the temperature of the inner wall is essentially uniform. At rest, the temperature is uniform in the system and the temperature experienced cycles between these two extreme conditions as shown in Fig 1d. In our previous studies of complex unit cell geometries [12, 13] we have demonstrated that the constraint of the pedestals and surrounding material require the outer and inner wall to deform by the same amount in the plane of the walls and not to experience any curvature. In 2D, the behaviour under these circumstances can be replicated by applying an iso-strain boundary condition and an appropriate temperature field on the 2-bar structure shown in Fig 1c. In the remainder of this and in the following sections, we explore the response of this idealisation to provide insight into the range of phenomena that can occur under practical loading conditions. This idealisation does not include the effect of impingement and film holes. We explore how they influence the behaviour in section 5.

2.1 Governing equations

The kinematic boundary condition in Fig 1c requires that the two walls experience the same total strain, such that at any instance, τ , of the loading cycle, the strain at any position, y , in the hot wall is related to the strain in the cool wall by:

$$\frac{\sigma_h(y, \tau)}{E} + \alpha T_h(y, \tau) + \varepsilon_{p_h}(y, \tau) = \frac{\sigma_c(\tau)}{E} + \alpha T_{min}(\tau) + \varepsilon_{p_c}(\tau) \quad (1)$$

where E is Young's modulus, α is the thermal expansion coefficient, $\sigma_h(y, \tau)$, $\sigma_c(\tau)$ are the stresses in the hot and cool walls, respectively, and $\varepsilon_{p_h}(y, \tau)$, $\varepsilon_{p_c}(\tau)$ are the corresponding plastic strains; the stresses and plastic strains are uniform in the cool wall since the latter experiences a uniform temperature variation $T_{min}(\tau)$ through the cycle, whereas they are not uniform in the hot wall as the latter experiences a linear temperature distribution, $T_h(y, \tau) = \bar{T}_h(\tau) - y\Delta T_h(\tau)/t_h$, where $\bar{T}_h(\tau) = [T_{max}(\tau) + T_{med}(\tau)]/2$, is the average hot wall temperature.

Simultaneously, equilibrium in Fig 1c at full load, i.e. at instance τ_1 (see Fig 1d) implies:

$$\int_{-t_h/2}^{t_h/2} \sigma_h(y, \tau_1) dy + \sigma_c(\tau_1)t_c = p(t_c + t_h) \quad (\text{full load}) \quad (2i)$$

whereas equilibrium in Fig 1c at zero load, i.e. at instance τ_0 (see Fig 1d) gives:

$$\int_{-t_h/2}^{t_h/2} \sigma_h(y, \tau_0) dy + \sigma_c(\tau_0)t_c = 0 \quad (\text{zero load}) \quad (2ii)$$

where p is the maximum mechanical stress corresponding to the steady state regime of the cycle, i.e. $p = p(\tau_1) = p(\tau_{1'})$ in Fig 1d.

2.2 Elastic solution

A detailed description of the elastic solution for the system in Fig 1c is available in [15]. Here the solution is described briefly and is written in a compact form suitable for the shakedown calculations. Application of Eq 1 and Eq 2i for the hot wall mid plane, $y = 0$, in the elastic regime give:

$$\frac{\hat{\sigma}_{h_m}(\tau)}{E} + \alpha \bar{T}_h(\tau) = \frac{\hat{\sigma}_c(\tau)}{E} + \alpha T_{min}(\tau) \quad (3i)$$

$$\hat{\sigma}_{h_m}(\tau) \bar{t}_h + \hat{\sigma}_c(\tau) \bar{t}_c = p \quad (3ii)$$

where $\hat{\sigma}_{h_m}(\tau)$, $\hat{\sigma}_c(\tau)$ are the elastic membrane stress variations in the hot and cool walls, with $\bar{t}_c = t_c/(t_c + t_h)$ and $\bar{t}_h + \bar{t}_c = 1$. By solving Eq 3i-ii and adding the elastic bending stresses, $\hat{\sigma}_{h_b}(\tau) = E\alpha\Delta T_h(\tau)y/t_h$, in the hot wall (due to the zero total bending curvature of the system), we can write the elastic stresses in the walls at an instance, τ , as:

$$\hat{\sigma}_h(y, \tau) = -\sigma_T(\tau) \bar{t}_c \lambda + \sigma_T(\tau) \bar{\Delta T}_h \frac{y}{t_h} + p(\tau) \quad \text{and} \quad \hat{\sigma}_c(\tau) = \sigma_T(\tau) \bar{t}_h \lambda + p(\tau) \quad (4i)$$

where $\lambda = 1 - \bar{\Delta T}_h/2$ and $\sigma_T(\tau) = E\alpha\Delta T(\tau)$ is an indicator of the severity of thermal loading. The ratio $\bar{\Delta T}_h = \Delta T_h(\tau)/\Delta T(\tau)$ lies within $0 \leq \bar{\Delta T}_h \leq 1$ and is constant during the cycle because $\Delta T_h(\tau)$ and $\Delta T(\tau)$ vary proportionately, i.e. in Fig 1d we assume that the temperatures $T_{max}(\tau)$, $T_{med}(\tau)$ and $T_{min}(\tau)$ vary in-phase. In our analysis we will refer to the instantaneous values of quantities during the thermomechanical loading by $\Delta T(\tau)$, $\sigma_T(\tau)$, $T_{max}(\tau)$, $T_{min}(\tau)$ and $p(\tau)$, whereas the peak values corresponding to the steady state regime of the cycle will be referred to as ΔT , σ_T , T_{max} , T_{min} and p (see Fig 1d). In this notation, the steady state elastic stresses in the walls are:

$$\hat{\sigma}_h(y) = -\sigma_T \bar{t}_c \lambda + \sigma_T \bar{\Delta T}_h \frac{y}{t_h} + p \quad \text{and} \quad \hat{\sigma}_c = \sigma_T \bar{t}_h \lambda + p \quad (4ii)$$

2.3 Material model

We consider three material models with the following characteristics.

- A. Constant yield stress, σ_y (and no creep).
 - B. Temperature dependent yield stress calibrated for the CMSX-4 Ni alloy and illustrated again here in Fig 2a. No creep is included.
 - C. The above temperature dependent yield stress model with creep behaviour included; the latter was also calibrated for the CMSX-4 Ni alloy and is shown again here in Fig 2b.
- Perfect plasticity and pressure independent yield is considered in all the models. For models B and C, the yield stress in the cold regime ($T < T_{tr} = 700$ °C) is $\sigma_{y_0} = 805$ MPa (see Fig 2a), and in the

hot regime ($T > 720$ °C) is $\sigma_{y_T} = c_1 T + c_2$, with $c_1 = -1.88$ MPa/°C, $c_2 = 2336$ MPa. For model C, the creep power law:

$$\dot{\epsilon}_{cr} = \dot{\epsilon}_0 \operatorname{sgn}(\sigma) \left(\frac{|\sigma|}{\sigma_0} \right)^n \exp(x) \quad (5)$$

describes the creep strain rate, $\dot{\epsilon}_{cr}$, versus constant stress, σ , for the isothermal data in Fig 2b in uniaxial loading, with $x = -\frac{Q}{R} \left(\frac{1}{T} - \frac{1}{T_0} \right)$ and creep constants $\dot{\epsilon}_0 = 1/h$, $\sigma_0 = 800$ MPa, $T_0 = 830$ °C, $n = 10$, $Q = 400$ KJ/mol and $R = 8.31$ (J/mol·K).

In our shakedown calculations with model A, Young's modulus, E , and thermal expansion coefficient, α , are constant and we normalise the results, such that the values of E , α and σ_y do not need to be specified. When models B and C are used, we take the reference values, $\alpha = 1.74 \cdot 10^{-5}$, $E = 100$ GPa for CMSX-4 at 700 °C and also apply appropriate correction factors as follows. We scale the above value of E by the factor $1/(1 - \nu)$, to account for the increase of thermal stresses in the actual 3D walls of Fig 1b with respect to the 2D plane stress problem in Fig 1c; a reference Poisson's ratio, $\nu = 0.4$, is used. We also multiply the above value of α by 1.4, as this has been found to account for the increase of thermal stresses due to the increase of α by ~50% from room temperature to 1100 °C and the decrease of E by ~40% in CMSX-4 [15, 26]. The above corrections imply that the constant, augmented value of $E\alpha = 4.06$ MPa/°C is used in the definition of thermal stress $\sigma_T = E\alpha\Delta T$. Variations of E and α through the loading cycle will be considered in a later study.

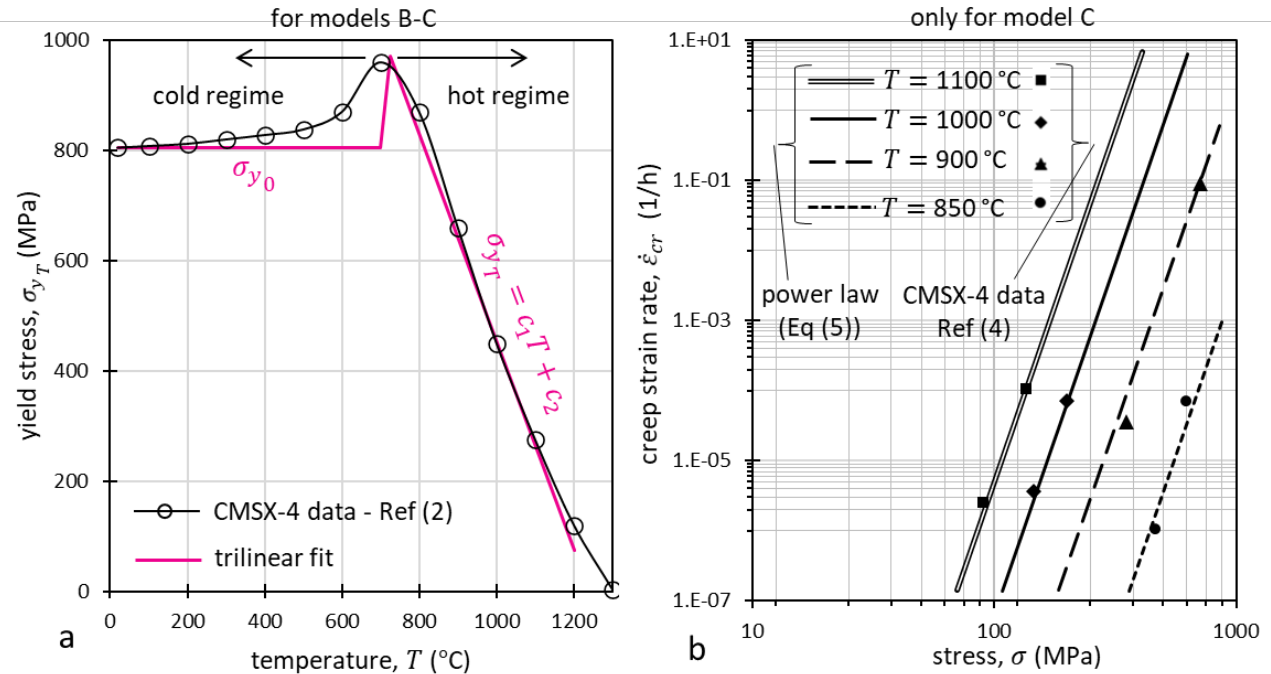


Figure 2. (a) Temperature dependent yield stress models B and C calibrated for CMSX-4. (b) Power law creep model C, calibrated for CMSX-4 based on isothermal creep rate data at different stress levels. Reproduced from [2].

3. Construction of interaction diagrams

This section describes major steps in the calculations for the determination of boundaries between different types of behaviour such as between elastic shakedown and reversed plasticity. We also consider the underpinning shakedown theory and describe a strategy for determining ratchet mechanisms and the boundaries between ratchetting and other types of behaviour.

3.1 Limit load

Determination of the limit load, p_L , for this particular configuration is straightforward. For material model A (fixed yield stress), p_L is determined by using $\sigma_h(y) = \sigma_c = \sigma_y$ in Eq 2a, giving $p_L = \sigma_y \bar{t}_h + \sigma_y \bar{t}_c$. This corresponds to a vertical line in a Bree type (Brussels) interaction diagram with axes of normalised maximum mechanical stress, p/σ_y , and normalised maximum thermoelastic stress, σ_T/σ_y , as shown in Fig 5-6. For models B and C we need to identify the instant in the cycle that gives the lowest collapse load. The temperature dependent yield stress in the hot wall, $\sigma_{y_h}(y)$, and cool wall, σ_{y_c} , can be expressed in terms of the peak thermoelastic stress amplitude, σ_T , by:

$$\sigma_{y_h}(y) = c_1 T_{max} + c_2 - \frac{c_1}{E\alpha} \overline{\Delta T}_h \left(0.5 + \frac{y}{t_h} \right) \sigma_T \quad (6a)$$

$$\sigma_{y_c} = c_1 T_{max} + c_2 - \frac{c_1}{E\alpha} \sigma_T \quad (6b)$$

Applying Eq 2i provides three possible expressions for the limit load:

$$\int_{-t_h/2}^{t_h/2} \sigma_{y_h}(y) dy + \sigma_{y_c} t_c = p_L(t_c + t_h) \quad (L1)$$

$$\int_{-t_h/2}^{t_h/2} \sigma_{y_h}(y) dy + \sigma_{y_0} t_c = p_L(t_c + t_h) \quad (L2)$$

$$\int_{-t_h/2}^{y_{tr}} \sigma_{y_h}(y) dy + \sigma_{y_0} \left(\frac{t_h}{2} - y_{tr} \right) + \sigma_{y_0} t_c = p_L(t_c + t_h) \quad (L3)$$

In L1 both walls yield in the hot yield strength regime (this occurs for high T_{max} and low ΔT), in L2 the cool wall yields in the cold yield strength regime (the hot remains in the hot regime) and in L3 a position, $y_{tr} = t_h(T_{max} - T_{tr})/(\overline{\Delta T}_h \Delta T) - t_h/2$, exists below which the inner fibres of the hot wall also yield in the cold yield strength regime (due to high $\overline{\Delta T}_h$) along with the cool wall. The L1, L2 and L3 limits for material models B-C are plotted in the interaction diagrams of Figs 7a-f with normalised axes $\sigma_T/\bar{\sigma}_y$ and $p/\bar{\sigma}_y$, where $\bar{\sigma}_y = 500$ MPa is an approximate average yield stress over the practical range of interest.

3.2 Shakedown-reverse plasticity boundary (SP)

We now determine the boundary between the elastic shakedown regime, here denoted as ‘S’, and the regime where a location exists within the structure that experiences reversed plastic straining during the cycle, here referred to as reverse plasticity or plastic shakedown and denoted by ‘P’. In the absence of creep, this boundary, referred to as ‘SP’, is determined by simply requiring that the elastic stress range at any location touches the yield surface at the two extremes of the cycle. Here the two possible locations for reverse plasticity are the outer fibre of the hot wall and the entire cool wall. The elastic stress range at these locations is equivalent to the absolute values of the steady state elastic solutions in Eq 4ii, such that the corresponding elastic shakedown-reverse plasticity (SP) boundaries for model A are given by:

$$|\hat{\sigma}_c| = p^s + \bar{t}_h \sigma_T^s \lambda = 2\sigma_y \quad \text{cool wall} \quad (\text{SPc})$$

$$|\hat{\sigma}_h(y = -t_h/2)| = \sigma_T^s \bar{t}_c \lambda + 0.5 \sigma_T^s \overline{\Delta T_h} - p^s = 2\sigma_y \quad \text{hot wall at } y = -t_h/2 \quad (\text{SPh})$$

For model B the yield stress range, $2\sigma_y$, must be replaced by $2\sigma_{y_0}$ for SPc and by $\sigma_{y_0} + \sigma_{y_h}(y = -t_h/2)$ for SPh. In the interaction diagrams here, the SP boundary for the system is constructed as the inner envelope of the individual SPc and SPh boundaries corresponding to the cool wall and outer fibre of the hot wall, as shown in Figs 5-7.

3.3 Elastic shakedown-ratchet boundary (SR)

Here we determine the boundary between elastic shakedown (S) and ratchetting (R), again in the absence of creep, denoted as ‘SR’. It is essential here to consider Koiter’s kinematic upper bound theorem [27] which states that the system will ratchet or experience reverse plastic straining if a mechanism of compatible plastic strains can be found over a given loading cycle, such that the total work done by the elastic stress variations over the cycle is greater than the total plastic energy dissipation over the cycle.

By assuming that plastic strains accumulate at two discrete instances, τ_i and τ_j , through the cycle, the above theorem is expressed in a modified form. We firstly write the elastic stress variations, $\hat{\sigma}_h(y, \tau)$ and $\hat{\sigma}_c(\tau)$ in the two walls (Eq 4i), as a function of the maximum (steady state) stresses at the SR boundary, σ_T^s, p^s , as:

$$\hat{\sigma}_h(y, \tau) = c(\tau) p^s - d(\tau) \left(\bar{t}_c \lambda - \overline{\Delta T_h} \frac{y}{t_h} \right) \sigma_T^s \quad \text{and} \quad \hat{\sigma}_c(\tau) = c(\tau) p^s + d(\tau) \bar{t}_h \lambda \sigma_T^s \quad (7)$$

where $c(\tau)$ and $d(\tau)$ depend on the detailed form of the cycle (Fig 1d) and satisfy $c(\tau) = d(\tau) = 0$ when the instance, τ , corresponds to zero load (instance 0 in Fig 1d) and $c(\tau) = d(\tau) = 1$ when τ corresponds to full load (instance 1 in Fig 1d). We now consider that in the general case of a thermal gradient, ΔT_h , through the hot wall, different parts of the hot wall will undergo plasticity at different instances through the cycle, i.e. the outer fibres lying between the outer edge position $y = -t_h/2$ and a given position $y = a$, will experience plastic strain at instance, τ_i , whereas the remainder of the hot wall (between $y = a$ and the inner edge position $y = t_h/2$) will experience plastic strain at instance, τ_j , together with the cool wall. If $\hat{\sigma}_h^s(y, \tau_i)$, $\hat{\sigma}_h^s(y, \tau_j)$ and $\hat{\sigma}_c^s(\tau_j)$ are the elastic stress

values of Eq 7 at the SR boundary, then for the current problem Koiter's theorem can be written in the following general form:

$$\begin{aligned} \int_{-\frac{t_h}{2}}^a \hat{\sigma}_h^s(y, \tau_i) d\varepsilon_{p_h}(y, \tau_i) dy + \int_a^{\frac{t_h}{2}} \hat{\sigma}_h^s(y, \tau_j) d\varepsilon_{p_h}(y, \tau_j) dy + \hat{\sigma}_c^s(\tau_j) d\varepsilon_{p_c}(\tau_j) t_c \\ \leq \int_{-\frac{t_h}{2}}^a \sigma_{y_h}(y, \tau_i) d\varepsilon_{p_h}(y, \tau_i) dy + \int_a^{\frac{t_h}{2}} \sigma_{y_h}(y, \tau_j) d\varepsilon_{p_h}(y, \tau_j) dy + \sigma_{y_c}(\tau_j) d\varepsilon_{p_c}(\tau_j) t_c \quad (8) \end{aligned}$$

where $d\varepsilon_{p_h}(y, \tau_i)$, $d\varepsilon_{p_h}(y, \tau_j)$ and $d\varepsilon_{p_c}(\tau_j)$ are the plastic strain increments in the outer hot wall fibres, the inner hot wall fibres and the cool wall, respectively, associated with the assumed mechanism at the two instances τ_i and τ_j of the cycle, and $\sigma_{y_h}(y, \tau_i)$, $\sigma_{y_h}(y, \tau_j)$, $\sigma_{y_c}(\tau_j)$ are yield stresses corresponding to these locations and instances.

Eq 8 provides an upper bound to the SR boundary which only depends on the form of the mechanism and not its scale. It is constructed as the inner envelope of the lines corresponding to all the possible mechanisms. When a mechanism is such that τ_i corresponds to the removal of the thermal and mechanical loads, e.g. instance 0 in Fig 1d, then the respective terms $c(\tau_i)$ and $d(\tau_i)$ are equal to zero, but the corresponding plastic energy dissipation term remains.

In the present problem, the derivation the SR boundary generally requires two equations: an equilibrium equation at full load (instance 1 in Fig 1d) to provide a relationship between the position, $y = a$, and the thermomechanical loads σ_T^s and p^s , and the modified Koiter upper bound theorem (Eq 8). The position, $y = a$, separates the two regions of the hot wall that undergo plasticity at different instances of the cycle (see for example Fig 3a) and therefore is the position of the elastic-plastic interface in the hot wall.

3.4 Reverse plasticity-ratchet boundary (PR)

We now consider the 'PR' boundary that separates the reverse plasticity (P) and ratchetting (R) regimes in the absence of creep. Eq 8 cannot be used in its current form for this purpose because now all the possible associated ratchet mechanisms that determine the inner envelope which defines the PR boundary, involve a volume of material that undergoes significant reverse plastic straining during a cycle. Ponter [28, 29] has developed an extended shakedown method for these circumstances, which determines the PR boundary by excluding the volume subjected to reverse plasticity and employing Eq 8 for the reduced structure, whilst scaling the elastic stresses at the left of the inequality based on a suitably chosen residual stress field. However, here we will not use this method for two reasons. Firstly, in the current problem where thermal loading is severe, Ponter's method can provide an overly conservative estimate of the PR boundary because it assumes that the volume subjected to reverse plasticity hardens to an elastic state [28, 29]; the latter is not the case for the Ni alloys of interest here and also conflicts with our idealisation of perfectly plastic material behaviour. Secondly, a preliminary study by the authors [16] has revealed that in the coupled wall structure, there exist possible mechanisms where plasticity does not occur at the two load extremes of the cycle (instances 1 and 0 in Fig 1d), but instead plastic strain can accumulate at an unknown instance, κ , during loading

or unloading due to the temperature dependence of the yield strength. In these cases, application of Ponter's method requires additional considerations.

The PR boundary is determined here by an extended Bree type analysis, underpinned by the governing kinematic (Eq 1) and equilibrium (Eq 2) relations for the twin wall system. The PR boundary corresponding to the most complex mechanisms here is determined by a system of four equations with three unknowns; these unknowns need not be found since only a relationship between σ_T^s and p^s is sought. The equations involve two equilibrium and two kinematic relationships corresponding to the two instances of plasticity. Similar to the derivation of the SR boundary, an equilibrium equation at full load is required to determine the position, $y = a$, of the elastic-plastic interface as a function of σ_T^s and p^s . A universal feature introduced by Bree [17] and used here is that the slope of the stress distribution in the elastic region of the hot wall is always of magnitude $\sigma_T(\tau)\bar{\Delta T}_h/t_h$ (see elastic solution - Eq 4i), such that the stress in this region, at an instance, τ , is written as $\sigma_h(\xi, \tau) = \pm \sigma_{y_h}(y = a, \tau) \pm \xi \sigma_T(\tau)\bar{\Delta T}_h/t_h$, where ξ is a local position measured from the elastic-plastic interface (denoted later in Figs 3a-g) and $\sigma_{y_h}(y = a, \tau)$ is the yield stress at the elastic-plastic interface, $y = a$. Another general feature that applies only at the boundary of a ratchet mechanism is that the position, $y = a$, experiences zero plastic strain through the cycle. Thus, the two kinematic relations (one at full load and one at zero load) are conveniently formed between the cool wall and the position, $y = a$; however, this changes for mechanisms where plasticity does not occur at the two load extremes, as it will be later shown in Section 4. In all kinematic relations it is essential to express the temperature in terms of σ_T ; here we use $T_h(y, \tau) = T_{max}(\tau) - \frac{\bar{\Delta T}_h}{E\alpha} \left(0.5 + \frac{y}{t_h}\right) \sigma_T(\tau)$ and $E\alpha(T_{max}(\tau) - T_{min}(\tau)) = E\alpha\Delta T(\tau) = \sigma_T(\tau)$.

3.5 Boundaries associated with creep deformation

So far, creep deformation has been ignored. Generally, creep acts in synergy with plasticity, increasing the inelastic strain accumulation in the structure over a cycle and therefore enhancing ratchetting and cyclic plasticity. This moves the SP, SR and PR boundaries to lower thermal and mechanical loads, σ_T and p , as well as introducing additional potential global creep failure and creep-ratchet mechanisms. The scale of these effects primarily depends on the applied temperature levels and the duration they are maintained per cycle. Here we assume that creep only occurs during the steady state period of the cycle, i.e. between instances, 1 and 1' (see Fig 1d), designated here as the 'creep dwell' period, t_{dwell} .

In order to modify a boundary that corresponds to a given loading range, $\sigma_T - p$, we firstly consider whether creep deformation at the given range is local or global. At large thermal differences, ΔT , i.e. large σ_T , creep is localised at the high temperature locations of the system, i.e. the outer fibres of the hot wall; here modifications can be done based on the estimation of the amount of local stress relaxation during t_{dwell} , by using the constitutive creep law (Eq 5). At moderate ΔT values, i.e. moderate σ_T , significant creep deformation can occur in the entire hot wall; for high p loads this can activate additional creep-ratchet mechanisms, the scale of which is evaluated by determining the steady creep-ratchetting state of the structure by using the creep law along with equilibrium and kinematic relations for the cyclic state. Lastly, at low ΔT values, i.e. low σ_T , creep can also occur in

the cool wall; this can activate a global creep failure mechanism, the scale of which is determined in a similar manner to the creep-ratchetting mechanism above.

3.6 Strategy for assuming ratchet mechanisms

Our strategy for determining a ratchet mechanism is to firstly consider all the possibilities of plastic straining at the two load extremes (full load and zero load) that can occur as the mechanical load, p , decreases from the limit load, down to zero load. This gives the assumed mechanism groups SR1, PR1, PR2 and SR2, illustrated physically in Figs 3a-d, which are classified in such an order that the elastic region in the hot wall, at full load, translates from the outer fibres ($y < 0$) towards the inner fibres ($y > 0$) as p decreases. For example, in group PR1 (Fig 3b) the lengths a and b that define the inner and outer elastic-plastic interfaces increase and decrease as p decreases; when the condition $a = t_h/2$ is reached in Fig 3b, the tensile plastic region in the hot wall vanishes and therefore the mechanism group PR2 is activated; the same applies between SR1 and PR1 as well as between other mechanism groups in Fig 3. Our Bree type diagrams in Section 4, show that the transition between two mechanism groups implies graphically that the two non-linear boundaries of the two groups share a point of tangency.

Next, we consider the possibility of reverse plasticity in the cool wall, which arises in systems with low thickness ratio, t_c/t_h . We modify the already assumed mechanism groups SR1, PR1 and PR2 to satisfy the above condition, which gives the mechanisms groups PR3, PR4 and PR5, respectively. For these groups we also assume that the walls yield simultaneously during unloading at instance, κ , which is based on experience from our preliminary study [16] of structural situations with low t_c/t_h ratio.

We then consider simple mechanisms where an elastic-plastic interface in the hot wall does not exist, i.e. $a = t_h/2$, which arises at low thermal difference ratios, ΔT_h , in the hot wall. Thus, by simply postulating $a = t_h/2$ in the already assumed mechanism groups SR1, PR2, SR2 and PR5 of Fig 3, we respectively obtain the possible mechanisms SR1', PR2', SR2' and PR6 of Figs 4. Finally, we consider another two possibilities of plastic straining relevant to mechanism PR2' Fig 4b, which gives the mechanisms PR2'' (Fig 4c) and PR7 (Fig 4f).

groups of ratchet mechanisms

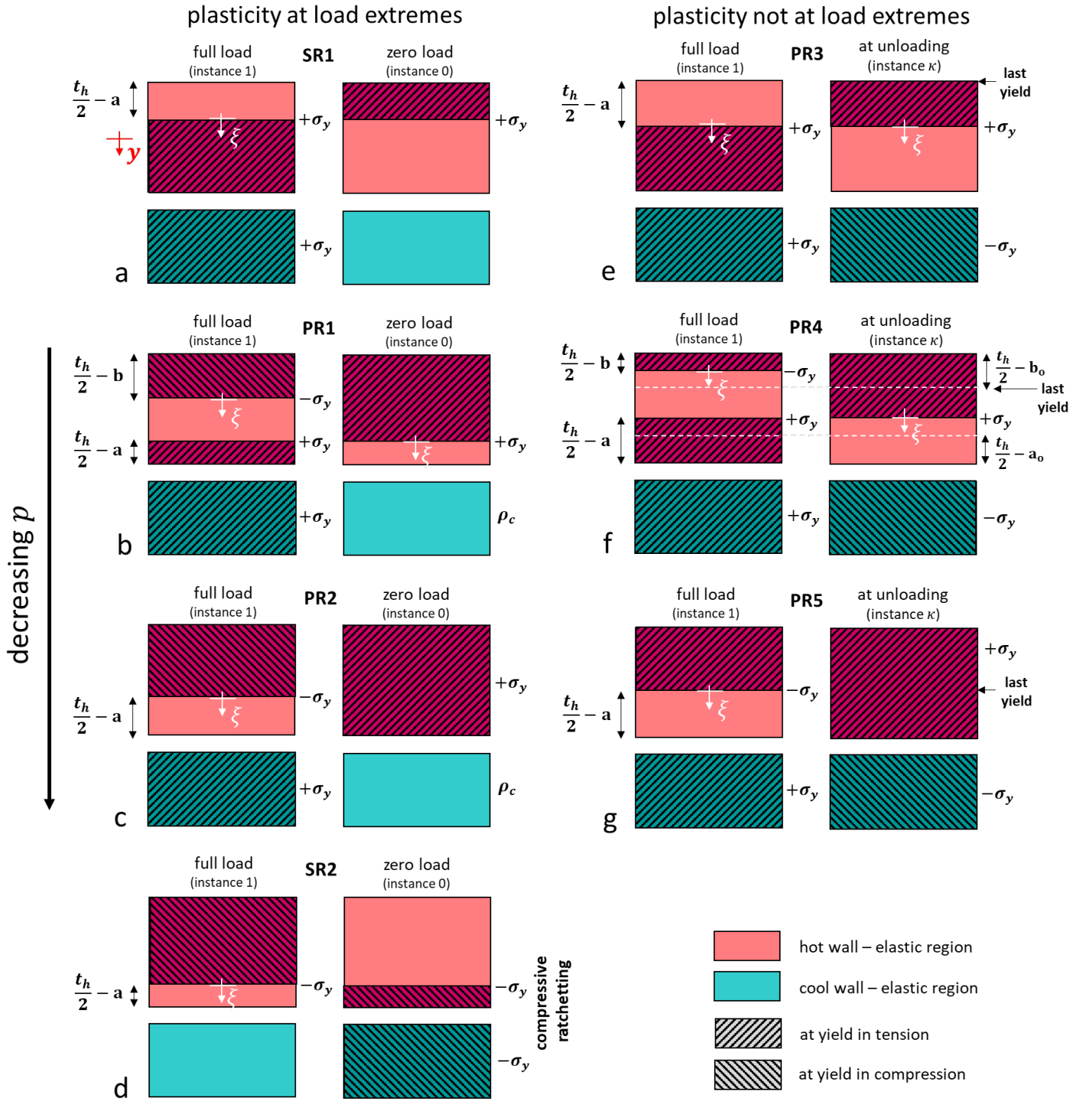


Figure 3. (a) Physical illustration of groups of ratchet mechanisms that occur in the general case of $\overline{\Delta T}_h > 0$ and constant yield stress, σ_y (material model A). In the left column plasticity occurs at the load extremes whereas in the right column plasticity occurs at full load and at an unloading instance, κ .

extreme ratchet mechanisms

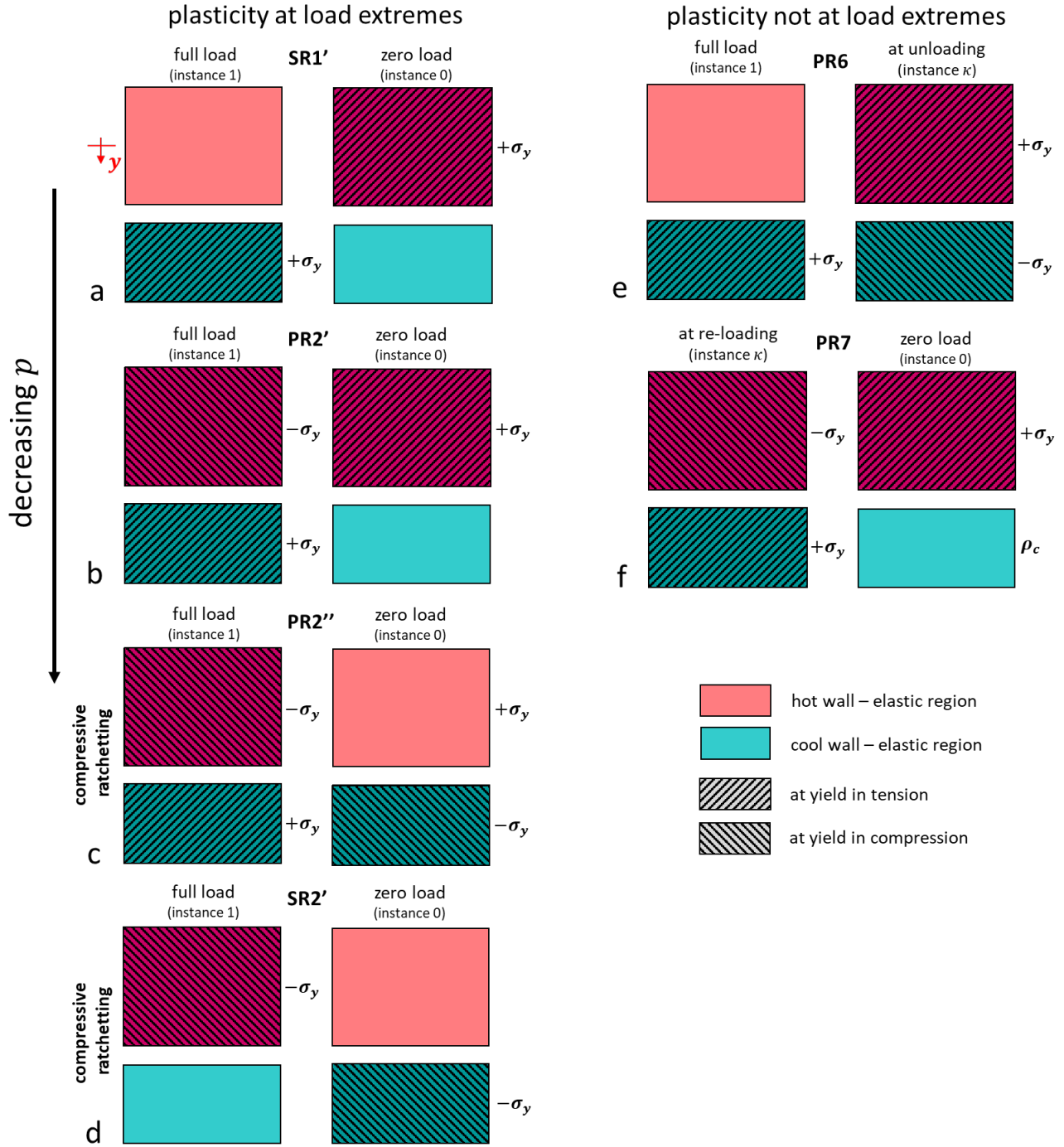


Figure 4. (a) Physical illustration of extreme cases of ratchet mechanisms where the entire hot wall yields; these occur at low $\Delta\bar{T}_h$ and have been determined in for $\Delta\bar{T}_h = 0$. SR1', PR2' and SR2' are extreme cases of SR1, PR2 and SR2 in Figs 4a,c,d. For illustration reasons a constant yield stress, σ_y , is used (material model A).

diagrams for $t_c/t_h = 1$

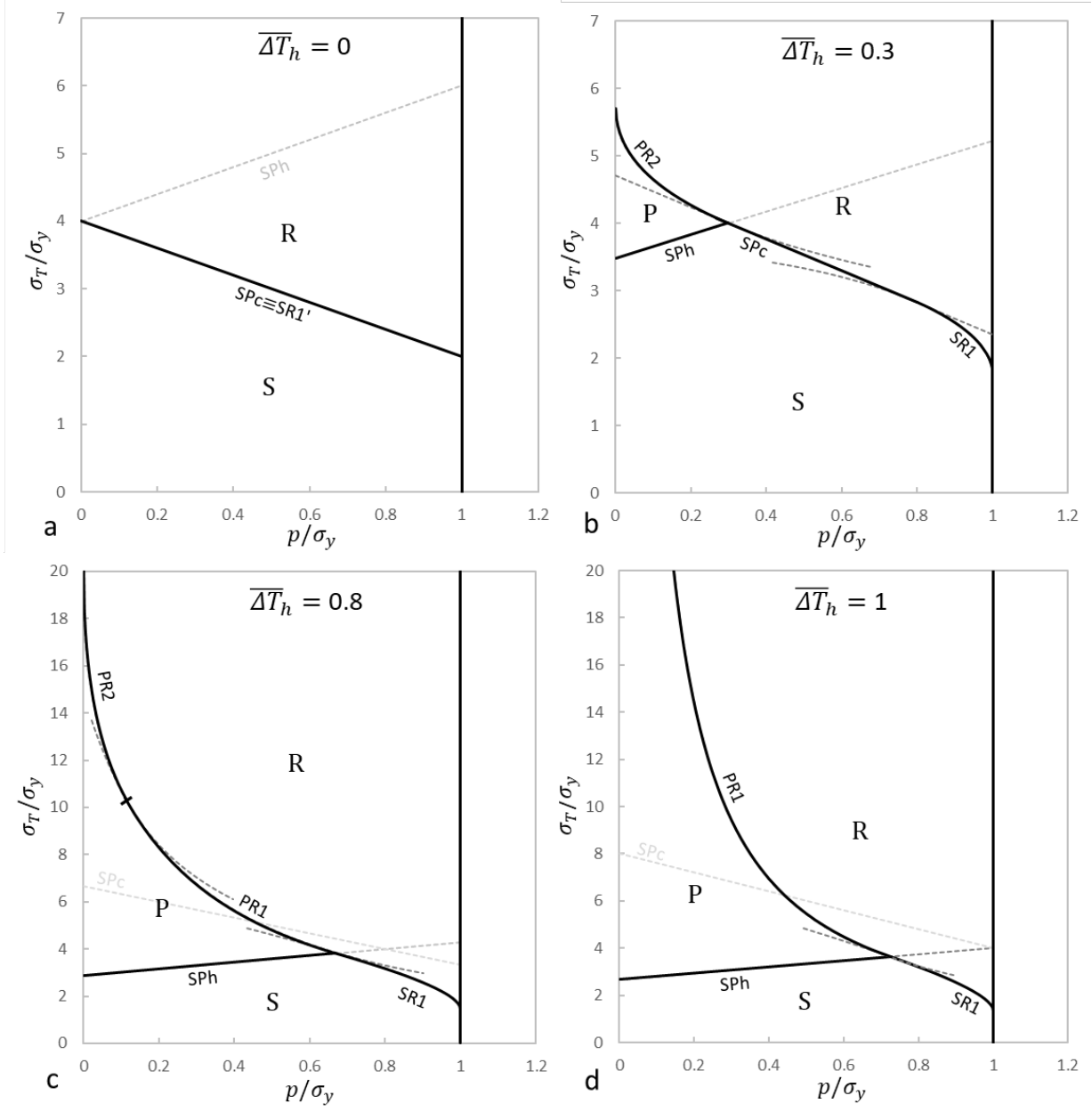


Figure 5. Interaction diagrams for constant yield stress (material model A) and $t_c/t_h = 1$, for varying $\overline{\Delta T}_h$: (a) $\overline{\Delta T}_h = 0$, (b) $\overline{\Delta T}_h = 0.3$, (c) $\overline{\Delta T}_h = 0.8$, and (d) $\overline{\Delta T}_h = 1$. Inactive ratchet boundaries and sections of SPh and SPc falling outside the inner envelope of SPh and SPc are denoted as grey dashed lines.

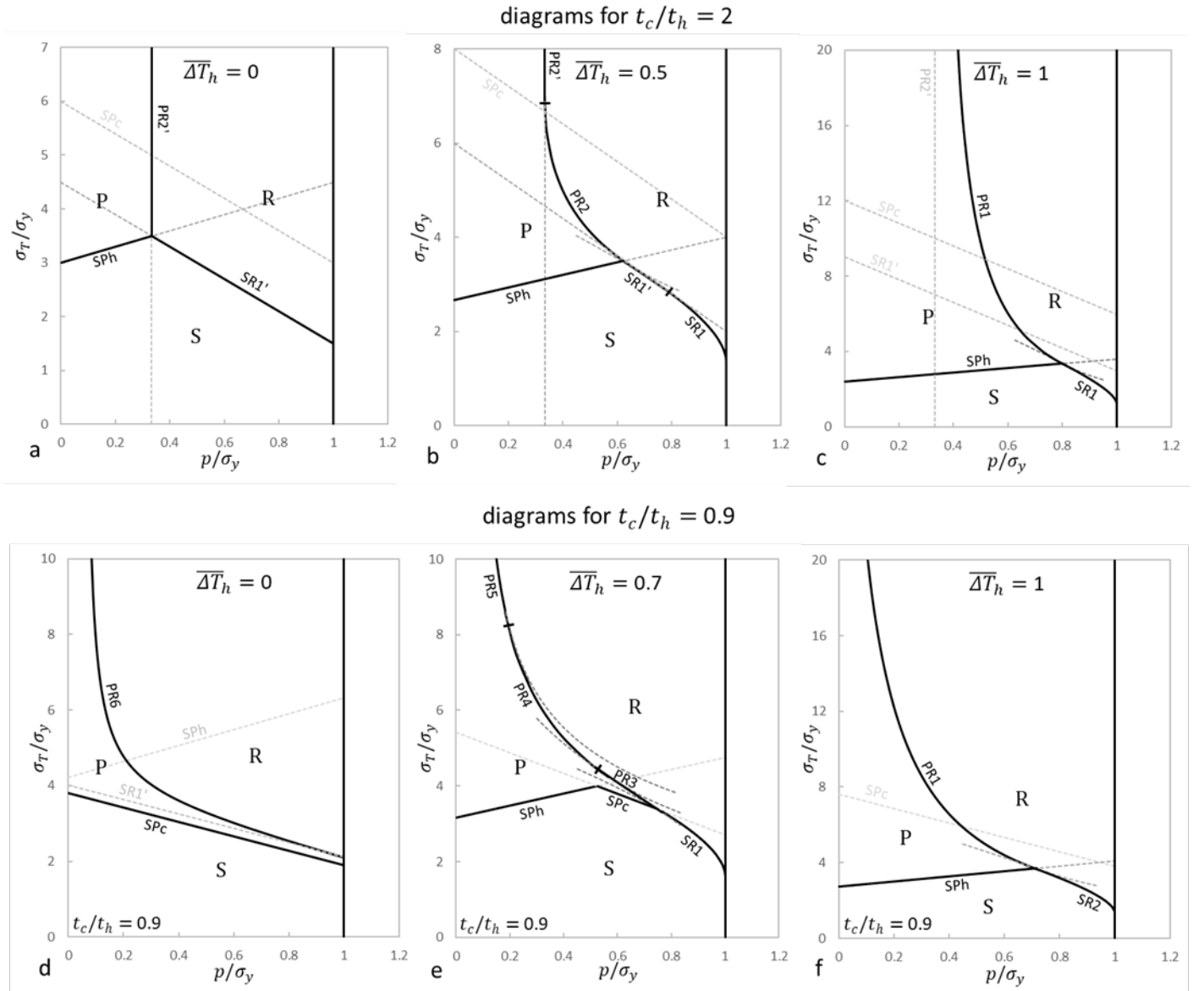


Figure 6. Interaction diagrams for constant yield stress (material model A) and the cases of $t_c/t_h = 2$ (a-c) and $t_c/t_h = 0.9$ (d-f), for varying ΔT_h . Inactive ratchet boundaries and sections of SPh and SPc falling outside the inner envelope of SPh and SPc are denoted in grey dashed lines.

$$T_{max} = 1100 \text{ }^{\circ}\text{C}, t_{dwel} = 1.96 \text{ h}$$

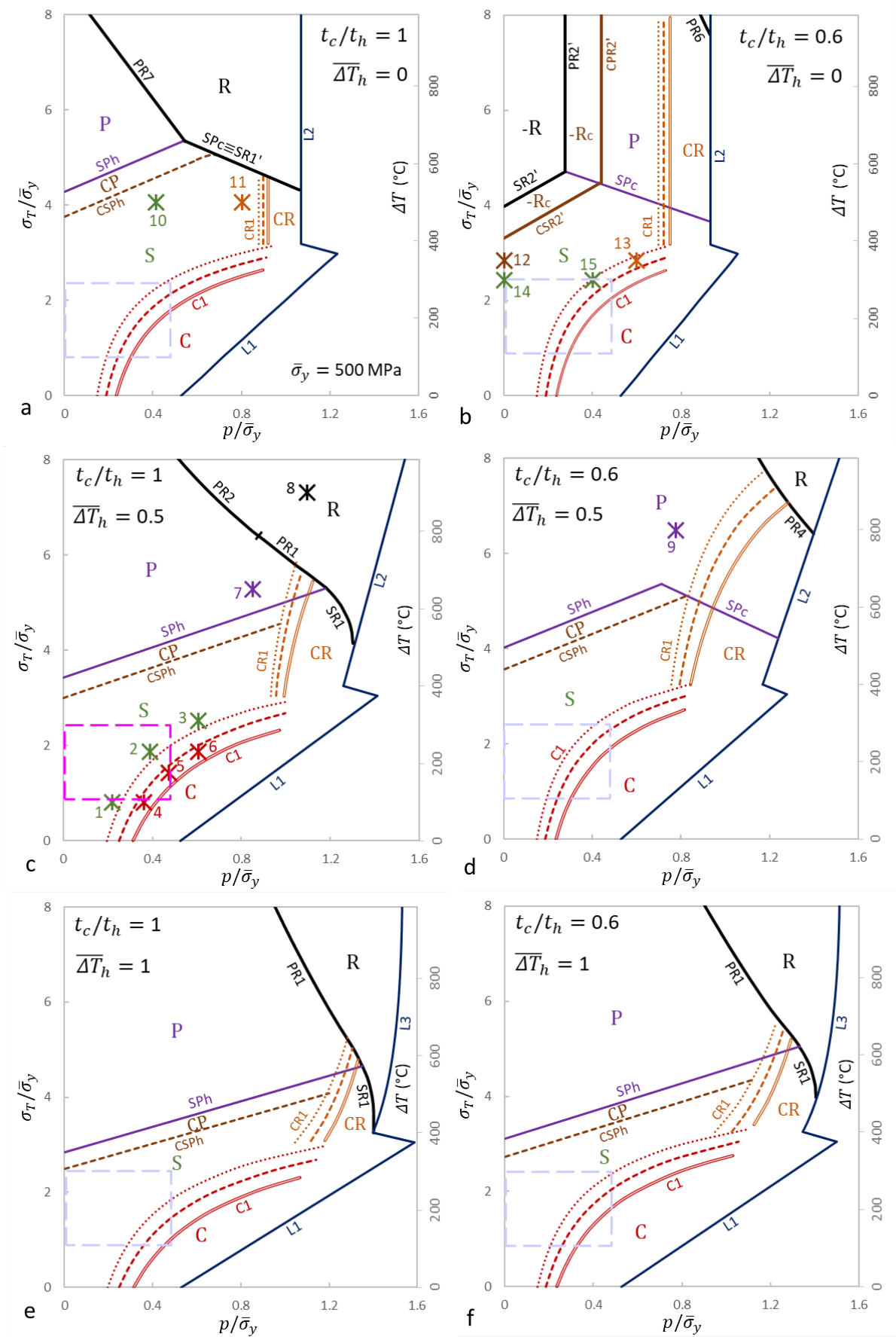


Figure 7. Interaction diagrams for material models B and C (temperature dependent yield stress with creep (C) and no creep (B)) for varying wall thickness ratio, t_c/t_h , and thermal gradient ratio, $\overline{\Delta T}_h$, and a fixed maximum temperature, $T_{max} = 1100 \text{ }^{\circ}\text{C}$. The CP, CR and C regimes are induced by creep (material model C). The mechanical and thermal loads, p and σ_T ($\sigma_T = E\alpha\Delta T$) are normalised by an average yield stress, $\bar{\sigma}_y = 500 \text{ MPa}$. The pink box in Fig 6d indicates the practical loading range of interest in current double wall transpiration cooled designs.

4. Derivation of ratchet and creep-associated boundaries

In this section we employ the methodologies described in Sections 3.3-3.5 to derive all the ratchet boundaries that correspond to the assumed mechanisms illustrated in Figs 3-4 and described in Section 3.6. The ratchet and creep-associated boundaries deduced here are plotted in the Bree type interaction diagrams of Figs 5-8; each diagram corresponds to a particular wall thickness ratio and temperature field conditions. To help the reader, the derivations here are presented for the simple case of a constant yield stress, i.e. $\sigma_{y_h}(y, \tau) = \sigma_{y_c} = \sigma_y$ (material model A), which is also consistent with the unique term, σ_y , used in Figs 3-4 for each mechanism; for the extended derivations corresponding to a temperature dependent yield stress (material model B) the reader is referred to the Appendices.

4.1 Derivation of shakedown-ratchet boundaries (material models A-B)

4.1.1 Elastic shakedown-ratchet boundaries SR1 and SR1'

SR1 is a 2nd order polynomial boundary determined by using equilibrium at full load (Eq 2i) for Fig 3a:

$$\int_{-(\frac{t_h}{2}-a)}^0 \left(\sigma_y + \xi \sigma_T^s \frac{\overline{\Delta T}_h}{t_h} \right) d\xi + \sigma_y \left(\frac{t_h}{2} + a \right) + \sigma_y t_c = p^s(t_c + t_h) \quad (i)$$

and Koiter's shakedown theorem (Eq 8): (SR1)

$$\int_{-a}^{t_h/2} \hat{\sigma}_h^s(y, \tau_1) dy + \hat{\sigma}_c^s(\tau_1) t_c = \sigma_y t_h + \sigma_y t_c \quad (ii)$$

where the elastic solutions, $\hat{\sigma}_h^s(y, \tau_1)$, $\hat{\sigma}_c^s(\tau_1)$ are given by Eq 7 and ξ is the local position measured from the elastic-plastic interface (denoted in Figs 3a-g). The extreme case of $a = -t_h/2$ in Fig 3a is equivalent to the SR1' mechanism in Fig 4a; by postulating this condition a linear SR1' boundary is obtained only by using Eq SR1(ii). Figs 5a-b and 6a-b show that the transition of the active ratchet mechanism of the system from SR1 into SR1' occurs either due to a decreasing p or $\overline{\Delta T}_h$. It is also noted that for $t_c/t_h = 1$ (Figs 5a-b) SR1' coincides with the shakedown-reverse plasticity boundary SPc. Appendix A gives the extended SR1(i-ii) relationships for material model B.

4.1.2 Reverse plasticity-ratchet boundary PR1

PR1 is a 2nd order polynomial boundary determined by using equilibrium at full load for Fig 3b:

$$-\sigma_y \left(\frac{t_h}{2} - b \right) + \int_0^{a+b} \left(-\sigma_y + \xi \sigma_T^s \frac{\overline{\Delta T}_h}{t_h} \right) d\xi + \sigma_y \left(\frac{t_h}{2} - a \right) + \sigma_y t_c = p^s(t_c + t_h) \quad (i)$$

equilibrium at zero load (Eq 2b):

$$\sigma_y \left(\frac{t_h}{2} + a \right) + \int_0^{\frac{t_h}{2}-a} \left(\sigma_y - \xi \sigma_T^s \frac{\overline{\Delta T}_h}{t_h} \right) d\xi + \sigma_c(\tau_0) t_c = 0 \quad (ii)$$

kinematics (Eq 1) between $y = a$ and the cool wall at full load: (PR1)

$$\frac{\sigma_y}{E} + \alpha T_h(y = a, \tau_1) = \frac{\sigma_y}{E} + \alpha T_{min} + \varepsilon_{p_c}(\tau_1) \quad (iii)$$

kinematics between $y = a$ and the cool wall at zero load:

$$\frac{\sigma_y}{E} = \frac{\sigma_c(\tau_0)}{E} + \varepsilon_{p_c}(\tau_1) \quad (iv)$$

as well as by considering that within the length of the elastic region, $a + b$ (see Fig 3b) the stress changes by $2\sigma_y$, such that $\sigma_T^s \overline{\Delta T}_h / t_h = 2\sigma_y / (a + b)$. The quantities $\varepsilon_{p_c}(\tau_1)$, $\sigma_c(\tau_0)$ are plastic strain accumulated at full load in the cool wall and the corresponding residual stress at zero load. Figs 5d, 6c, 6f and 7e-f demonstrate that PR1 is an active mechanism group only at large $\overline{\Delta T}_h$. Appendix B gives the extended PR1 (i-iv) relationships for material model B.

4.1.3 Reverse plasticity-ratchet boundaries PR2 and PR2', PR2''

PR2 is a 2nd order polynomial boundary determined by using equilibrium at full load for Fig 3c:

$$-\sigma_y \left(\frac{t_h}{2} + a \right) + \int_0^{\frac{t_h}{2}-a} \left(-\sigma_y + \xi \sigma_T^s \frac{\overline{\Delta T}_h}{t_h} \right) d\xi + \sigma_y t_c = p^s(t_c + t_h) \quad (i)$$

equilibrium at zero load:

$$\sigma_y t_h + \sigma_c(\tau_0) t_c = 0 \quad (ii)$$

kinematics between $y = a$ and the cool wall at full load: (PR2)

$$-\frac{\sigma_y}{E} + \alpha T_h(y = a, \tau_1) = \frac{\sigma_y}{E} + \alpha T_{min} + \varepsilon_{p_c}(\tau_1) \quad (iii)$$

and kinematics between $y = a$ and the cool wall at zero load:

$$\frac{\sigma_y}{E} = \frac{\sigma_c(\tau_0)}{E} + \varepsilon_{p_c}(\tau_1) \quad (iv)$$

As p decreases, the extreme condition, $a = t_h/2$ occurs in Fig 3c, i.e. the elastic region in the hot wall vanishes. In this case the extreme mechanism PR2' is activated (Fig 4b) and a completely vertical boundary prevails (Fig 6b), which is determined by using $a = t_h/2$ in Eq PR2(i). This condition of reverse plasticity (P) in the entire hot wall (Fig 4b) is promoted at large wall thickness ratios, i.e. $t_c/t_h > 1$. At thickness ratios $t_c/t_h < 1$, the mechanism PR2'' (Fig 4c) is activated instead of PR2', which involves the same plastic straining with PR2' at full load and therefore its boundary is given by the same relationship. It differs, however, in that reverse plasticity occurs in the cool wall and therefore ratchetting occurs in the compressive direction (see Fig 4c and -R region in Fig 7b). Appendix C gives the extended PR2 (i-iv) relationships for material model B.

4.1.4 Elastic shakedown-ratchet boundaries SR2 and SR2'

SR2 and SR2' (Figs 3d, 4d) are boundaries that separate an elastic shakedown regime (S) from a compressive ratchetting (-R) regime (see -R region in Fig 7b). The -R regime is here found to occur only for a temperature dependent yield stress (material model B) and when t_c/t_h and $\overline{\Delta T}_h$ are simultaneously low (Fig 7b). SR2 is determined by using equilibrium (for model B) at full load for Fig 3d:

$$-\int_{-\frac{t_h}{2}}^a \sigma_{y_h}(y, \tau_1) dy + \int_0^{\frac{t_h}{2}-a} \left(-\sigma_{y_h}(y = a, \tau_1) + \xi \sigma_T^s \frac{\overline{\Delta T}_h}{t_h} \right) d\xi + \sigma_c(\tau_1)t_c = p^s(t_c + t_h) \quad (i)$$

kinematics between $y = a$ and the cool wall at full load: (SR2)

$$-\frac{\sigma_y}{E} + \alpha T_h(y = a, \tau_1) = \frac{\sigma_c(\tau_1)}{E} + \alpha T_{min} \quad (ii)$$

and Koiter's shakedown theorem (Eq 8):

$$\int_{-\frac{t_h}{2}}^a |\hat{\sigma}_h^s(y, \tau_1)| dy = \int_{-\frac{t_h}{2}}^a \sigma_{y_h}(y, \tau_1) dy + \int_a^{\frac{t_h}{2}} \sigma_{y_h}(y, \tau_0) dy + \sigma_{y_c}(\tau_0)t_c \quad (iii)$$

Since instance τ_0 corresponds to zero load, the condition $\sigma_{y_h}(y, \tau_0) = \sigma_{y_c}(\tau_0) = \sigma_{y_0}$ applies, i.e. yielding at the cold yield strength. The particular case of an SR2' boundary (Fig 4d) is determined by using $a = t_h/2$ in Eq SR2(iii) only.

4.1.5 Reverse plasticity-ratchet boundary PR3

PR3 is a 4th order polynomial boundary determined by equilibrium at full load for Fig 3e:

$$\int_{-(\frac{t_h}{2}-a)}^0 \left(\sigma_y + \xi \sigma_T^s \frac{\overline{\Delta T}_h}{t_h} \right) d\xi + \sigma_y \left(\frac{t_h}{2} + a \right) + \sigma_y t_c = p^s(t_c + t_h) \quad (i)$$

equilibrium at the unloading instance, τ_k :

$$\sigma_y \left(\frac{t_h}{2} - a \right) + \int_0^{\frac{t_h}{2}+a} \left(\sigma_y - \xi k \sigma_T^s \frac{\overline{\Delta T}_h}{t_h} \right) dy - \sigma_y t_c = k p^s(t_c + t_h) \quad (ii)$$

kinematics between $y = a$ and the cool wall at full load: (PR3)

$$\frac{\sigma_y}{E} + \alpha T_h(y = a, \tau_1) = \frac{\sigma_y}{E} + \alpha T_{min} + \varepsilon_{p_c}(\tau_1) \quad (iii)$$

and kinematics between $y = -t_h/2$ (last yield location) and the cool wall at the unloading instance, τ_k :

$$\frac{\sigma_y}{E} + k \alpha T_{max} = -\frac{\sigma_y}{E} + k \alpha T_{min} + \varepsilon_{p_c}(\tau_1) \quad (iv)$$

One key difference here in comparison to the systems of equations for the PR1 and PR2 boundaries is that the unknown residual stress, $\sigma_c(\tau_0)$ (that can be determined by the system) is replaced by the load/temperature scaling factor, k , corresponding to the unknown instance, τ_k . Another difference is that the sequencing of plastic straining here is important, such that the last location that reaches yield on unloading, $y = -t_h/2$, must be used in Eq PR3(iv) instead of the elastic plastic interface $y = a$. Our interaction diagrams indicate that PR3 is active only for a constant yield stress (model A) and when $t_c/t_h < 1$ (see Fig 6e), such that the cool wall undergoes reverse plasticity.

4.1.6 Reverse plasticity-ratchet boundary PR4

PR4 is a boundary determined by equilibrium at full load for Fig 3f:

$$-\sigma_y \left(\frac{t_h}{2} - b \right) + \int_0^{a+b} \left(-\sigma_y + \xi \sigma_T^s \frac{\overline{\Delta T}_h}{t_h} \right) d\xi + \sigma_y \left(\frac{t_h}{2} - a \right) + \sigma_y t_c = p^s(t_c + t_h) \quad (i)$$

equilibrium at the unloading instance, τ_k :

$$\sigma_y \left(\frac{t_h}{2} + a \right) + \int_0^{\frac{t_h}{2}-a} \left(\sigma_y - \xi k \sigma_T^s \frac{\overline{\Delta T}_h}{t_h} \right) dy - \sigma_y t_c = k p^s(t_c + t_h) \quad (ii)$$

kinematics between $y = a$ and the cool wall at full load:

(PR4)

$$\frac{\sigma_y}{E} + \alpha T_h(y = a, \tau_1) = \frac{\sigma_y}{E} + \alpha T_{min} + \varepsilon_{p_c}(\tau_1) \quad (iii)$$

and kinematics between $y = -b_i$ (last yield) and the cool wall at the unloading instance, τ_k :

$$\frac{\sigma_y}{E} + k \alpha T_h(y = -b_i, \tau_1) = -\frac{\sigma_y}{E} + k \alpha T_{min} + \varepsilon_{p_c}(\tau_1) \quad (iv)$$

This derivation takes into account that the last yielding location, $y = -b_i$, at the instance, τ_k (see Fig 3f), does not coincide with the elastic-plastic interface, $y = -b$, at full load. This is because the latter changes position during loading such that within the elastic region indicated in Fig 3f at full load, there exists a region (between $y = -b$ and the upper dashed line) which in fact experiences plastic strain earlier in the cycle. Note that this effect also occurs in PR1 (Fig 3b) but it was not considered in the derivation of the ratchet boundary (Section 3.2.2) because the sequencing of plastic straining at unloading is not important. More details on this aspect and the derivation of b_i are provided in Appendix D. The solution of Eqs PR4(i-iv) leads to a quintic expression that is solved numerically to determine the PR4 boundary.

4.1.7 Reverse plasticity-ratchet boundary PR5

PR5 is a 2nd order polynomial boundary determined by equilibrium at full load for Fig 3g:

$$-\sigma_y \left(\frac{t_h}{2} + a \right) + \int_0^{\frac{t_h}{2}-a} \left(-\sigma_y + \xi \sigma_T^s \frac{\overline{\Delta T}_h}{t_h} \right) d\xi + \sigma_y t_c = p^s(t_c + t_h) \quad (i)$$

equilibrium at the unloading instance, τ_k :

$$\sigma_y t_h - \sigma_y t_c = k p^s(t_c + t_h) \quad (ii)$$

kinematics between $y = a$ and the cool wall at full load: (PR5)

$$-\frac{\sigma_y}{E} + \alpha T_h(y = a, \tau_1) = \frac{\sigma_y}{E} + \alpha T_{min} + \varepsilon_{p_c}(\tau_1) \quad (iii)$$

and kinematics between $y = a$ (last yield) and the cool wall at the unloading instance, τ_k :

$$\frac{\sigma_y}{E} + k\alpha T_h(y = a, \tau_1) = -\frac{\sigma_y}{E} + k\alpha T_{min} + \varepsilon_{p_c}(\tau_1) \quad (iv)$$

4.1.8 Reverse plasticity-ratchet boundary PR6

PR6 is a particular ratchet mechanism (Fig 4e), previously identified by the authors [16] for cases of low wall thickness ratios, $t_c/t_h < 1$ and zero thermal gradient through the hot wall, $\overline{\Delta T}_h = 0$ (see Fig 6d). PR6 has a highly non-linear boundary which has been determined based on the elastic solution and the yielding conditions at the unloading instance, k . Here we provide a more general derivation for $\overline{\Delta T}_h > 0$. Equilibrium at full load in Fig 4e gives:

$$\int_0^{t_h} \left(-\sigma_h(y = -t_h/2, \tau_1) + \xi \sigma_T^s \frac{\overline{\Delta T}_h}{t_h} \right) d\xi + \sigma_y t_c = p^s(t_c + t_h) \quad (i)$$

equilibrium at the unloading instance, τ_k :

$$\sigma_y t_h - \sigma_y t_c = k p^s(t_c + t_h) \quad (ii)$$

kinematics between $y = -t_h/2$ and the cool wall at full load: (PR6)

$$-\frac{\sigma_h(y = -t_h/2, \tau_1)}{E} + \alpha T_{max} = \frac{\sigma_y}{E} + \alpha T_{min} + \varepsilon_{p_c}(\tau_1) \quad (iii)$$

and kinematics between $y = -t_h/2$ and the cool wall at the unloading instance, τ_k :

$$\frac{\sigma_y}{E} + k\alpha T_{max} = -\frac{\sigma_y}{E} + k\alpha T_{min} + \varepsilon_{p_c}(\tau_1) \quad (iv)$$

where $\sigma_h(y = -t_h/2, \tau_1)$ is the stress in the hot wall at $y = -t_h/2$, which here is within yield.

4.1.9 Reverse plasticity-ratchet boundary PR7

PR7 is another particular ratchet mechanism (Fig 4f), that was identified previously by the authors [16] for the case of $\overline{\Delta T}_h = 0$ (see Fig 7a). Through FE analysis here we find that PR7 is indeed active only at $\overline{\Delta T}_h = 0$ and when the temperature dependent yield stress is used (model B). A derivation of the PR7 boundary based on equilibrium and kinematic relationships is not straightforward because the instance, τ_k , when the walls yield simultaneously occurs during re-loading (Fig 4f), i.e. the mechanism is activated after the first loading cycle. The boundary is conveniently determined by the method shown in [16] based on the elastic solution and the yielding conditions at the instance, $\tau_{k'}$; this is also provided here in Appendix E.

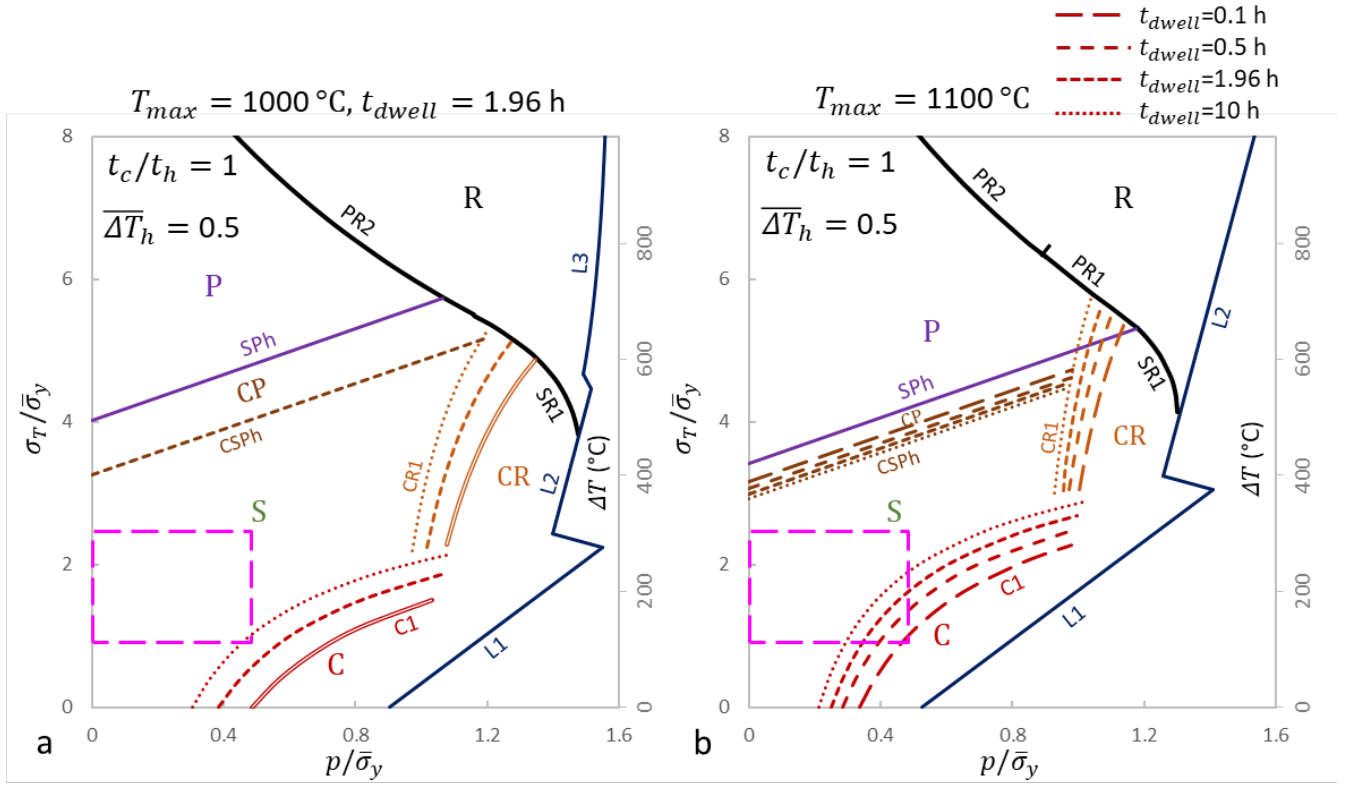


Figure 8. Interaction diagrams showing the effect of maximum temperature, T_{max} , and creep dwell time, t_{dwell} , on the CP, CR and C regimes induced by creep (material models B and C). (a) Maximum temperature, $T_{max} = 1000\text{ °C}$ and fixed creep dwell time, $t_{dwell} = 1.96\text{ h}$. (b) Maximum temperature, $T_{max} = 1100\text{ °C}$ and varying t_{dwell} between 0.1 h, 0.5 h, 1.96 h and 10 h. A wall thickness ratio, $t_c/t_h = 1$, and thermal gradient ratio, $\Delta T_h = 0.5$ are used in both Figs 8a-b.

4.2 Derivation of creep-associated boundaries (material model C)

We now consider the material model C in order to determine how creep deformation influences the structural response by modifying the ratchet boundaries derived so far and by inducing additional creep failure mechanisms.

4.2.1 Creep-plasticity regime (CP)

The so called creep-plasticity regime, denoted as ‘CP’, is of local character as it occurs at large thermal differences, ΔT , i.e. large σ_T , and low mechanical loads, p , where compressive creep strain is localised at the outer fibres of the hot wall, during the creep dwell period, t_{dwell} , i.e. the remainder of the structure does not creep. The CP regime here spans all the load combinations for which the outer fibre of the hot wall ($y = -t_h/2$) experiences compressive creep strain during t_{dwell} and equal tensile plastic strain on unloading, and therefore is an intermediate regime between the elastic shakedown (S) and classical reverse plasticity (P) regimes (see Figs 7a-f). The corresponding boundary CSPh (Fig 7 for $t_{dwell} = 1.96\text{ h}$) is determined by deducting the amount of stress relaxation, $\Delta\sigma_{hcr}$, due to creep from the yield stress range used in the equation of the boundary SPh between elastic shakedown and reverse plasticity (in Section 3.2), as below:

$$\sigma_T^s \bar{t}_c \lambda + 0.5 \sigma_T^s \Delta T_h - p^s = \sigma_{y_0} + \sigma_{y_h}(y = -t_h/2) - \Delta\sigma_{hcr} \quad (\text{CSPh})$$

The analytical calculation of $\Delta\sigma_{hcr}$ is exact when $\overline{\Delta T}_h = 0$ [16], because in this case the hot wall is at a uniform temperature and therefore creeps at a uniform rate, $\dot{\epsilon}_{cr}$. For the general case $\overline{\Delta T}_h > 0$, $\dot{\epsilon}_{cr}$ varies through the hot wall thickness and therefore an analytical solution is not possible. An approximate calculation of $\Delta\sigma_{hcr}$ is provided in Appendix F.

4.2.2 Creep enhanced compressive ratchetting regime (-R_c)

The creep enhanced compressive ratchetting regime, denoted here as -R_c, occurs at similar loading combinations as the creep-plasticity regime (CP), described above, such that creep does not occur in the cool wall. The difference here is that compressive creep deformation at high temperature is no longer localised, but occurs in the entire hot wall due to a very low temperature gradient through its thickness, i.e. very low $\overline{\Delta T}_h$ in the current context. Under these circumstances, compressive creep strain accumulation during t_{dwell} , can activate the compressive ratchetting mechanisms PR2' and SR2', shown in Figs 4b and 4d, in the same manner as compressive plasticity in the hot wall on full load. These creep-induced mechanisms are referred to here as PR2'c and SR2'c and the corresponding boundaries are shown in Fig 7b for $\overline{\Delta T}_h = 0$. Similar to the construction of CSPh, these boundaries are determined by compensating for the amount of stress relaxation, $\Delta\sigma_{hcr}$ (calculated in Appendix F) during t_{dwell} , as in the derivations performed earlier for PR2' (Section 4.1.3) and SR2' (Section 4.1.4) for material model B. Considering that PR2' and SR2' are given by using $a = t_h/2$ in Eq PR2(i) and Eq SR2(ii), respectively, the creep-induced boundaries for $\overline{\Delta T}_h = 0$ are given by:

$$-(\sigma_{y_h} - \Delta\sigma_{hcr})t_h + \sigma_{y_0}t_c = p^s(t_c + t_h) \quad (\text{CPR2}')$$

$$|\hat{\sigma}_h|t_h = (\sigma_{y_h} - \Delta\sigma_{hcr})t_h + \sigma_{y_0}t_c \quad (\text{CSR2}')$$

Note that for $\overline{\Delta T}_h = 0$ the elastic solution $\hat{\sigma}_h$ given by Eq 4ii and the temperature dependent yield stress, σ_{y_h} , are not functions of position, y .

4.2.3 Creep ratchetting regime (CR)

The creep ratchetting regime, designated here as CR, has similar features to the -R_c regime described above, in that creep deformation occurs in the hot wall and no creep occurs in the cool wall. The difference is that CR requires severe mechanical loads, p , near the structural limit load, where tensile stresses dominate in the system at high temperature; therefore, the entire hot wall does not need to creep at high temperature for creep ratchetting to occur. For large thermal gradients in the hot wall, i.e. $\overline{\Delta T}_h = 1$, the cool wall and a portion of the hot wall are at tensile yield at high temperature (as for example in Fig 3e) while creep also occurs in the hot wall. For moderate thermal gradients in the hot wall, i.e. $\overline{\Delta T}_h = 0.5$, the same conditions occur, with the difference that only the cool wall is at yield at high temperature (as for example in Fig 4a). In both circumstances, stress relaxation due to creep will cause any initially compressive stresses in the outer fibres of the hot wall to gradually become tensile at high temperature (within a number of cycles), to maintain equilibrium with the load p . As a result, after a transient response, a steady cyclic response is set-up where tensile creep occurs in the hot wall, but due to yielding of the remaining structure the stresses cannot relax.

For large gradients, i.e. $\overline{\Delta T}_h = 1$, the tensile creep strain accumulation in the outer, elastic-creeping fibres of the hot wall is accommodated by simultaneous, equal tensile plastic strain accumulation in the inner, yielding fibres of the hot wall and the cool wall (yielding occurs as in Fig 3e at full load) to satisfy kinematics. The same occurs at lower gradients, i.e. $\overline{\Delta T}_h = 0.5$, with the difference that the entire hot wall creeps, which is accommodated by yielding of the cool wall only. In both cases, when the steady cyclic response is reached, any fibre in the system at high temperature either creeps or yields at a constant rate that is independent of position. Since our analysis here concerns the steady cyclic response, and specifically the dwell period of the cycle in which the stresses, temperatures and strain rates are constant, the instance, τ , need not be considered in the following expressions.

In the most complex case of $\overline{\Delta T}_h = 1$, the fibre at the interface, $y = a_{cr}$, between the elastic-creeping and yielding regions in the hot wall (under cyclic state conditions), creeps at the constant rate, $\dot{\epsilon}_{cr}$, under a constant stress that is equal to the local yield stress, $\sigma_{y_h}(y = a_{cr})$; for the cases of Figs 7e-f here the yielding region is practically in the cold yield stress regime, such that $\sigma_{y_h}(y = a_{cr}) = \sigma_{y_0}$. Therefore, the creep law (Eq 5) for $y = a_{cr}$ can be written as:

$$\epsilon_{cr1\%} = N_{1\%} t_{dwell} \dot{\epsilon}_o \left(\frac{\sigma_{y_0}}{\sigma_o} \right)^n \exp \left[-\frac{Q}{R} \left(\frac{1}{T_h(y = a_{cr})} - \frac{1}{T_o} \right) \right] \quad (\text{CR1i})$$

where $N_{1\%}$ is the number of loading cycles (creep dwells) required for a total creep strain accumulation of $\epsilon_{cr1\%} = 0.01$. A common creep rate between $y = a_{cr}$ and any creeping fibre at location, y , also implies:

$$\sigma_{y_0}^n \exp \left[-\frac{Q}{R} \left(\frac{1}{T_h(y = a_{cr})} - \frac{1}{T_o} \right) \right] = \sigma_h(y)^n \exp \left[-\frac{Q}{R} \left(\frac{1}{T_h(y)} - \frac{1}{T_o} \right) \right] \quad (\text{CR1ii})$$

Eqs CR1(i-ii) give an expression for the stress distribution, $\sigma_h(y)$, in the elastic-creeping region, which is then fed into the equilibrium relationship:

$$\int_{-\frac{t_h}{2}}^{a_{cr}} \sigma_h(y) dy + \int_{a_{cr}}^{\frac{t_h}{2}} \sigma_{y_h}(y) dy + \sigma_{y_0} t_c = p^{CR} (t_c + t_h) \quad (\text{CR1iii})$$

to determine the CR1 lines in Figs 7a-f; we plot three lines that represent $N_{1\%} = 20000$, $N_{1\%} = 2000$ and $N_{1\%} = 200$ cycles (for increasing p) required for a total creep strain accumulation of $\epsilon_{cr1\%} = 0.01$, for a fixed $t_{dwell} = 1.96$ h; the term p^{CR} denotes the value of p at the CR1 line.

For the simpler case of $\overline{\Delta T}_h = 0.5$ in Figs 7c-d, where there is not a creep-plastic interface, Eq CR1(ii) is not required as the expression for $\sigma_h(y)$ is provided directly from Eq CR1(i), by replacing σ_{y_0} with $\sigma_h(y)$ and $T_h(y = a_{cr})$ with $T_h(y)$; also a_{cr} must be replaced by $t_h/2$ in CR1(iii). Generally, when $\overline{\Delta T}_h > 0$ the integration of $\sigma_h(y)$ needs to be done numerically. For $\overline{\Delta T}_h = 0$, the hot wall sees a uniform stress, i.e. $\sigma_h(y) = \sigma_h$ and the solution is analytical and gives linear CR1 boundaries (Figs 7a-b).

4.2.4 Global creep regime (C)

The global creep regime, designated here as C, differs from all the above regimes associated with creep (CP, -R_c and CR) in that due to a large T_{max} and simultaneously low ΔT , creep deformation also occurs in the cool wall. If a large enough mechanical load, p , is also applied, then after a transient period of stress relaxation and re-distribution over a number of cycles, a steady cyclic response prevails where the entire system creeps at a uniform, constant rate while the stress field remains constant (during t_{dwell}). Equilibrium and the requirement for a common creep rate between the walls respectively give:

$$\int_{-\frac{t_h}{2}}^{\frac{t_h}{2}} \sigma_h(y) dy + \sigma_c t_c = p^C (t_c + t_h) \quad (i)$$

(C1)

$$\sigma_h(y)^n \exp \left[-\frac{Q}{R} \left(\frac{1}{T_h(y)} - \frac{1}{T_o} \right) \right] = \sigma_c^n \exp \left[-\frac{Q}{R} \left(\frac{1}{T_{min}} - \frac{1}{T_o} \right) \right] \quad (ii)$$

where the term p^C denotes the value of p at the C1 boundary. Eqs C1(i-ii) provide an expression for the steady state stress in the cool wall, σ_c , which can then be fed into the creep failure relation:

$$\varepsilon_{cr_{0.1}} = N_{0.1} t_{dwell} \dot{\varepsilon}_o \left(\frac{\sigma_c}{\sigma_o} \right)^n \exp \left[-\frac{Q}{R} \left(\frac{1}{T_{min}} - \frac{1}{T_o} \right) \right] \quad (iii)$$

to construct the C1 contours in Figs 7a-f, representing $N_{1\%} = 20000$, $N_{1\%} = 2000$ and $N_{1\%} = 200$ (for increasing p at $\sigma_T = 0$) cycles for an accumulation of $\varepsilon_{cr_{1\%}}$ for fixed $t_{dwell} = 1.96$ h; also, for $\overline{\Delta T}_h > 0$ the integration of $\sigma_h(y)$ is numerical.

The calculation scheme associated with the global creep failure regime (C) and the creep ratchetting regime (CR) in Section 3.3.3, can be applied for any maximum temperature in the system, T_{max} , and any creep dwell period, t_{dwell} . To highlight the strong sensitivity of the CR1 and C1 boundaries, with respect to T_{max} , we provide the additional Figure 8a, corresponding to $T_{max} = 1000$ °C and compare it against Fig 7c, corresponding to $T_{max} = 1100$ °C; in both figures $t_{dwell} = 1.96$ h and the lines represent $N_{1\%} = 20000$, $N_{1\%} = 2000$ and $N_{1\%} = 200$ (for increasing p at $\sigma_T = 0$) cycles for an accumulation of $\varepsilon_{cr_{1\%}}$. To highlight the pronounced effect of t_{dwell} , we also provide Fig 8b, for $T_{max} = 1100$ °C, which compares the CR1 and C1 boundaries for four cases of interest to transpiration systems: $t_{dwell} = 0.1$ h, $t_{dwell} = 0.5$ h, $t_{dwell} = 1.96$ h and $t_{dwell} = 10$ h; here all the lines represent $N_{0.1} = 2000$ cycles required for $\varepsilon_{cr_{1\%}}$ accumulation.

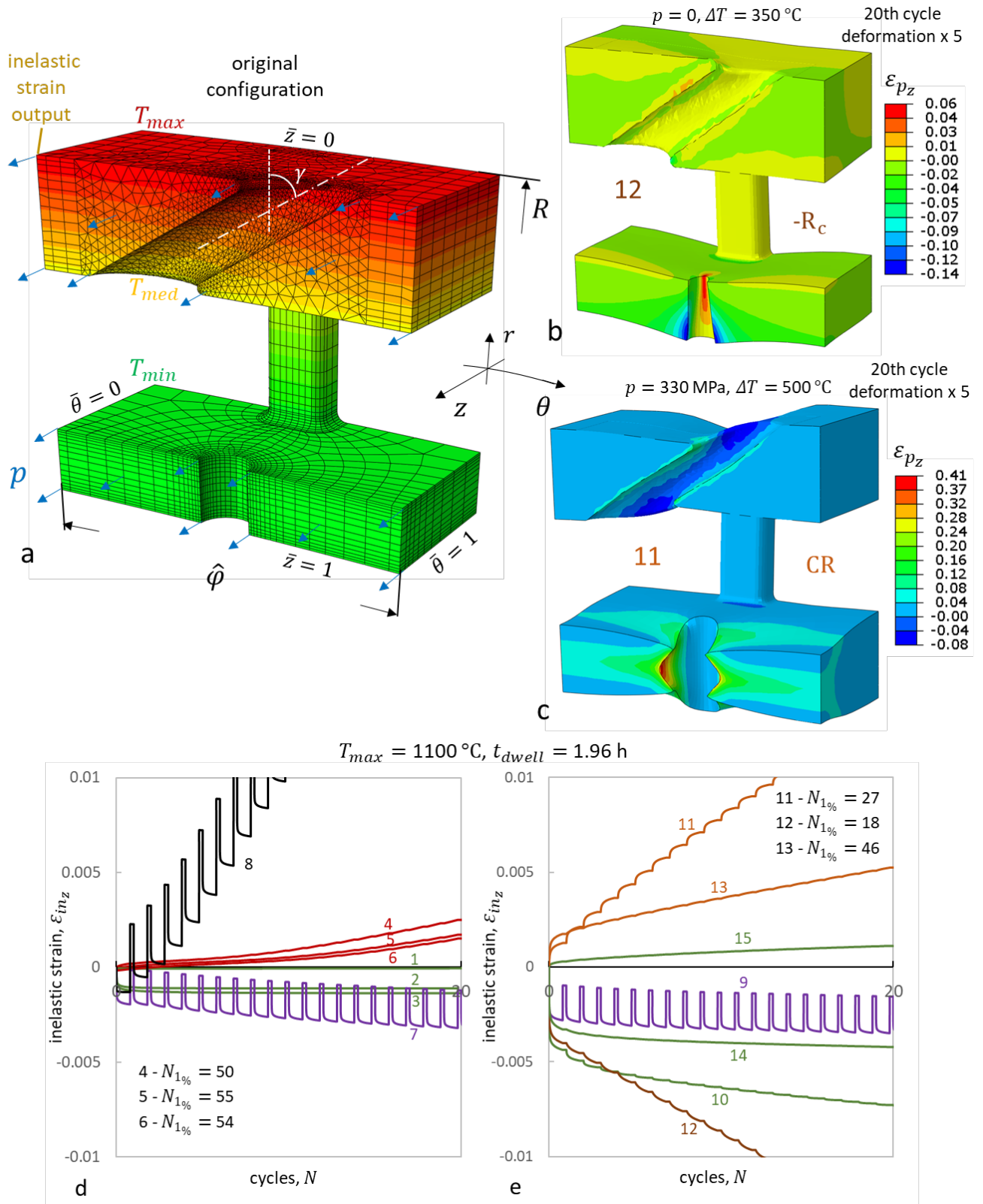


Figure 9. (a) Reduced 3D FE model used in cycle-by-cycle FE simulations in the creep-plastic range. (b) Distorted structure at the 20th cycle (deformation scale factor 5) due to compressive ratchetting failure under the load combination 12. (c) Distorted structure at the 20th cycle due to creep ratchetting (tensile) under the load combination 11; the contours in both d-c show inelastic strain. (d-e) Inelastic strain histories at the output location (denoted in Fig 9a) over 20 cycles for different load combinations; $N_{1\%}$ in Figs 9d-e denotes the predicted number of applied cycles for a total inelastic strain accumulation of 1%, based on the creep/ratchet rate output at the 20th cycle. The ABAQUS Implicit FE scheme is used for the material model C (Section 2.3) with a Von Mises yield surface. The mesh consists of $\sim 1.3 \times 10^4$ 8-node hexahedral elements (C3D8T) and $\sim 2 \times 10^4$ 4-node tetrahedral elements (C3D4T). The kinematic constraints, the cyclic temperature field, the cyclic surface traction, and the creep law are respectively applied via the MPC, UDSIP, DLOAD and UCREEP subroutines.

5. Validation of theoretical analysis by FE simulations

We now link our 2D analytical results (model in Fig 1c) to the behaviour of the actual 3D system with holes (Fig 1b) by performing inelastic cycle-by-cycle FE simulations (material model C) in the reduced, cylindrical double wall model of Fig 9a. We analyse fifteen combinations of thermomechanical loading, $\Delta T - p$, and $\overline{\Delta T}_h$, t_c/t_h , ratios, which are marked and numbered in the diagrams of Figs 7a-d. These analyses provide insight into two questions: a) whether the global failure mechanisms determined by 2D analysis in Fig 7 (R, -R_c, CR and C) occur in the same $\Delta T - p$ range in the actual 3D geometry with holes, and b) whether the 3D system is safe against these failure mechanisms in the practical loading $\Delta T - p$ range of interest for gas turbine blades. This range spans thermal differences of $100 < \Delta T < 300$ °C and centrifugal stresses of $0 < p < 250$ MPa [3], as denoted by the dashed box in Figs 7a-e. Due to the cooling characteristics of the system the thermal difference ratio cannot take values far different from $\overline{\Delta T}_h \approx 0.5$ [3]; thus, emphasis is given to the pink box in Fig 7c.

5.1 Description of 3D double wall FE model

The model in Fig 9a is an idealisation of the full unit cell in Fig 1b and is used here for computational efficiency purposes; it gives the same nominal stress field (absence of holes) with the model of Fig 1b due to the large ratio of radius of curvature over wall thickness, $R/t_h = 100$. The relevance of Fig 9a to the 2D model analysed so far (Fig 1c) is based on applying the same temperature field and equivalent kinematic constraints (zero θ -displacements at the symmetry planes $\bar{\theta} = 0$ and $\bar{\theta} = 1$, zero z -displacements at $\bar{z} = 0$ and common displacement $u_z \neq 0$ at $\bar{z} = 1$; note: the wall extensions/contractions along θ occur through the radial, r , rigid body translation of the system – see Fig 9a). Mechanical loading involves a maximum z –traction, p_{net} , applied uniformly at the net cross sections of the walls. If $S = \hat{\phi}[t_h(R - t_h/2) + t_c(R - t_h - H - t_c/2)]$ is the gross cross section of the walls and $S_{film} = D_{film}t_h/\cos\gamma$, $S_{imp} = D_{imp}t_c$ are the cross sections removed by the film and impingement holes at the $\bar{z} = 1$ plane (Fig 9a), then the applied net-section traction is $p_{net} = pS/(S - S_{film} - S_{imp})$, where p is the ‘nominal’ maximum stress that has been used so far in Sections 2-4. It is also used here to plot the FE data points on the Bree type diagrams. $D_{film} = D_{imp} = 0.5$ mm are the film and impingement hole diameters ($\gamma = 60^\circ$ is the film hole angle with respect to the wall plane), $H = 1.5$ mm is the pedestal height and $\hat{\phi} = 0.036$ rad is the arc-angle that determines the lengths of the walls in the repeating unit of Fig 9a. For fixed $t_h = 1$ mm the case of $t_c/t_h = 1$ implies $p_{net} = 1.27p$ whereas $t_c/t_h = 0.6$ gives $p_{net} = 1.31p$.

5.2 FE output

The FE data corresponding to the numbered markers in Figs 7a-d are plotted in Figs 9d-e in terms of the inelastic strain, ε_{in_z} , history (creep strain + plastic strain) experienced over 20 cycles, at the location indicated in Fig 9a. Since global deformation mechanisms are explored here, the inelastic strain output location is chosen away from the film hole, because within a few cycles it provides a clearer indication of whether there is a net strain accumulation per cycle, compared to locations where

cyclic plastic deformation occurs, i.e. the outer rim of the film hole. The colour of each inelastic strain history in Figs 9d-e and the corresponding marker in Figs 7a-d represent the regime of behaviour where the system operates; the green colour for elastic shakedown (S) concerns only the output location and not cyclic plasticity locations near holes.

In this context, the load combinations 1, 2 and 3 lead to elastic or plastic shakedown, as long as the entire structure is considered (see Fig 7c and Fig 9d). The combinations 4, 5 and 6 corresponding to lower ΔT and/or higher p lead to global creep failure (C – red) (see Fig 7c and Fig 9d). The above transition from the shakedown regime (S) to the C regime is in overall agreement with the C1 lines drawn from the 2D analysis. Agreement is also demonstrated by the results for the load combinations 7 and 8, which respectively give plastic shakedown P (reverse plasticity – purple) and ratchetting (R – black) – see Fig 7c and Fig 9d. The combinations 11 and 13 (Figs 7a-b and Fig 9e) result in creep ratchetting (CR – orange) in a $\Delta T - p$ range similar to the analytical 2D prediction. CR occurs at smaller p in 3D (11 and 13 data points) since the wall net section at the $\bar{z} = 1$ plane (Fig 9a) carries a mechanical stress, p_{net} , augmented by a factor of ~ 1.27 with respect to the nominal p value; note that Fig 9a is a conservative idealisation of the full unit cell in Fig 1b, as the latter involves a lower level of porosity; also, higher porosity in a turbine blade implies lower mass and therefore lower p . The distortion of the structure at the 20th cycle for load combination 11 (CR response) is shown in Fig 9c for a deformation scale factor 5; a local thinning ratchet mechanism is evident at the reduced net section of the cool wall, similar to one observed in a thin plate with a transverse hole [25]; the distortion at the hot wall is more complex due to the inclined shape of the film hole.

The load combination 12 (Fig 7b Fig 9d) confirms the occurrence of a compressive ratchetting regime enhanced by creep (-R_c – brown) at zero mechanical load, $p = 0$; the distorted structure at the 20th cycle is illustrated in Fig 9c. The -R_c regime occurs at ΔT below the 2D analytical CSR2' boundary as the latter does not account for the biaxial thermoelastic stress field and its variation near the holes, i.e. stress concentrations and zero stresses normal to the hole surfaces. For a slight reduction of ΔT , i.e. load combination 14 (Fig 7b Fig 9d), compressive ratchetting is avoided.

6. General discussion

6.1 2D results

The first highlight of our 2D theoretical analysis is that introducing a thermal difference across the hot wall, i.e. a finite value of $\overline{\Delta T}_h$, increases the size of the reverse plasticity regime (P) and decreases the ratchetting (R) regime (see Figs 5-8). Simultaneously, the reverse plasticity boundary SP_c for cyclic plastic deformation in the cool wall is raised while the corresponding boundary SP_h for cyclic plasticity on the hot side of the hot wall is drastically lowered. Therefore, the response becomes Bree-like [17, 30, 31] as $\overline{\Delta T}_h$ is increased (Figs 5-6); the Bree diagram for in-phase loading [30] can be reproduced by using $t_c/t_h = 0$ and $\overline{\Delta T}_h = 1$ in our analytical scheme. From a practical perspective, the results show that even in the idealised 2D geometry without stress concentration features, cyclic plastic deformation at the outer hot wall fibre is of most concern, particularly when the decrease of yield strength with temperature (model B) is considered (Figs 7a-f).

The second highlight is that by increasing the thermal gradient ratio $\overline{\Delta T}_h$ or the wall thickness ratio, t_c/t_h , the global creep failure (C regime) reduces, i.e. the C1 lines occur at lower ΔT (or σ_T) and higher p (compare C1 lines with respect to dashed box in Figs 7a-f). This is because both $\overline{\Delta T}_h$ and t_c/t_h increase the volume of material that experiences low temperatures, thus reducing the steady-state creep rate of the structure for a given mechanical stress, p . Although the 2D analysis alone shows that global creep deformation is important since the loading range of interest (dashed boxes in Fig 7) overlaps with the C1 curves in Figs 7c-d, these curves are for the extreme temperature, $T_{max} = 1100$ °C, and dwell time, $t_{dwell} \approx 2$ h. A decrease of T_{max} by 100 °C gives the response in Fig 8a ($T_{max} = 1000$ °C), where the creep regime (C) significantly reduces; decreasing t_{dwell} also reduces the severity of creep (Fig 8b), although the adverse effect occurs at long dwell times, i.e. $t_{dwell} = 10$ h. These results indicate that T_{max} is a key parameter in design.

The third highlight of our 2D analysis is that the creep-ratchetting (CR), and classical ratchetting (R) mechanisms occur at very large mechanical and thermal loads, far away from the practical loading range (box in Fig 7). The extreme case of zero thermal gradient through the hot wall, i.e. $\overline{\Delta T}_h = 0$, gives the most conservative ratchet and creep boundaries (Figs 7a-b) and can lead to compressive ratchetting, enhanced by creep ($-R_c$) at zero mechanical load and when the cool wall is thin, i.e. for $t_c/t_h < 1$ (Fig 7b). Values near $\overline{\Delta T}_h \approx 0.5$ (Figs 7c-f) are however expected to occur in practise, for which an $-R_c$ regime is unlikely, even for the extreme case of $T_{max} = 1100$ °C.

6.2 3D FE results

The 3D FE analysis (Fig 9a) verifies the above features in two ways: a) the classical ratchetting (R), compressive ratchetting ($-R_c$), creep ratchetting (CR) and global creep (C) mechanisms depend in the same manner on the combination of thermomechanical loading, $\Delta T - p$, and $\overline{\Delta T}_h$, t_c/t_h , ratios as in the 2D model, and, b) in the practical loading range (box in Fig 7c) the 3D porous structure remains safe against all these mechanisms, except for excessive creep deformation (type C failure). This demonstrates the power of the analytical route in providing physical insight into the regimes of behaviour and how these change with various parameters, as well as in aiding the interpretation of FE results and cost-effective use of FE analysis, e.g. in the absence a 2D analytical interaction diagram the FE output of cyclic strain accumulation for the load combinations 7 and 10 (see Figs 9d-e) could be misinterpreted as compressive ratchetting ($-R_c$). Based on knowledge of the form of the $-R_c$ mechanism and the diagrams in Figs 7a,c we exclude the possibility of such a mechanism to occur at these load combinations and $\overline{\Delta T}_h$ and t_c/t_h , ratios and our interpretation is that the structure will shakedown to a cyclic state.

The 3D FE analysis highlights that creep ratchetting (CR) and global creep (C) occur at lower mechanical loads, p , than the 2D analytical prediction as well as that compressive ratchetting ($-R_c$) occurs at lower ΔT . These modifications are associated with: a) the biaxial stress field that occurs in 3D in association with a Von Mises yield surface; b) the effect of holes in reducing the wall section that carries the nominal centrifugal stresses, p ; and c) the effect of holes (and pedestals) in perturbing the stress field over a certain distance that scales with their size. The latter implies that sharp stress gradients and complex stress states, including significant shear components, occur around hole and pedestal features. An analytical treatment of such effects within a shakedown analysis is in most

cases impossible, even for simple 3D geometries; this may be the reason why the influence of holes on ratchet boundaries has been mainly demonstrated in the literature through simple hole-plate models using direct numerical methods, such as the Linear Matching Method [32]. Furthermore, the degree to which the hole size/porosity influences the ratchet boundary has not been fully investigated; Zheng et al [33] studied the sensitivity of the ratchet boundary for radially perforated thick cylinders with respect to the ratio of cylindrical diameter to perforation/hole diameter and showed that for ratios beyond 10 the hole effect is negligible. Based on this we can anticipate here that in the actual geometry of Fig 1b where the total porosity induced by the holes is as low as 3.7% (and the pedestal density is also low), the resulting stress field perturbations will only slightly modify the Bree diagram corresponding to a 3D plate without holes. In the idealised model of Fig 9a the porosity is increased to 5.5% and the perturbations may start to become significant. The effect of porosity on ratchet boundaries will be explored in future studies.

A key effect associated with the presence of holes is that the higher local cyclic elastic stress range experienced at these features promotes reverse plastic straining at lower load levels than predicted by the 2D model. This effect can be captured through determination of the local stress concentration factor, SCF, at stress raisers, since it indicates how the local cyclic elastic stress range compares with the sum of the high and low temperature yield strength locally [2], which in turn determines the ‘true’ boundary (SP) between shakedown and reversed plasticity (Section 3.2). Through this approach we are able to illustrate in Figs 10a-b how the 2D analytical SPh boundary (and the associated CSPh boundary) reduces to low ΔT values due to the high SCF at the outer rim of the film hole, giving a new boundary designated as SPf; we also show that the SCF at the impingement hole imposes an additional boundary SPi, such that the actual SP boundary in the structure is given by the inner envelope of SPf and SPi. We define SCF here as the maximum hole stress (calculated by elastic 3D FE simulations in Fig 9a) normalised by the theoretical nominal stress in the θ –direction (given by Eq 4ii for $y = -t_h/2$ and $p = 0$). In agreement with [3], the SCF at the film hole is practically independent of wall thickness ratio, t_c/t_h , and reduces linearly with the p/σ_T ratio according to $\text{SCF} = 3.6 - 11 p/\sigma_T$, whereas the SCF at the impingement hole increases with p/σ_T ; here $\text{SCF} = 1.85 - 9 p/\sigma_T$. These explain the slopes of the SPf and SPi boundaries in Figs 10a-b; the boundaries are obtained by simply scaling the elastic stresses by SCF in the expressions of Section 3.2 (by using $p = 0$ as SCF is defined here based on the θ –nominal stress for convenience). Simultaneously, the reduction of the wall net section by the holes is considered in Figs 10a-b to cause a shift of the creep curves C1 to lower p values, the extent of which is determined by applying the scaling $p_{net} \approx 1.27p$.

The modified boundaries in Fig 10 now clearly indicate that the prominent damage mechanisms in the loading range of interest (dashed box) are: a) cyclic plastic deformation (which can lead to fatigue failure) at the outer film hole rim or the impingement hole surface (CP and P regimes), and, b) global creep deformation (C regime). These mechanisms can occur simultaneously, i.e. their boundaries overlap within the dashed box in Figs 10a-b. Creep deformation can be critical since for $\Delta T = 200$ °C and $t_c/t_h = 1$ a centrifugal stress $p = 200$ MPa is predicted to cause 1% creep strain in just 200 cycles and when $t_c/t_h = 0.6$ the same will occur if the stress is as little as $p = 125$ MPa. The significance of 1% creep strain in turbine blade design is discussed in [34]. On the other hand, the severity of cyclic plastic deformation at the rim of the film hole and how this leads to fatigue failure has been demonstrated and analysed by the authors in [2]. The present study confirms our

previous findings in terms of the significance of local failure processes and highlights the importance of creep. In this regard, a low thickness ratio, t_c/t_h , is found here to promote global creep deformation (compare C1 lines between Fig 10a and Fig 10b), potentially posing a limit to the extent by which t_c/t_h may be reduced in design for the purpose of delaying fatigue at the film hole. Moreover, although a low t_c/t_h reduces cyclic plasticity at the film hole, this is at the detriment of enhanced plasticity at the impingement hole (Figs 10a-b).

An aspect which can enhance ratchetting is the out-of-phase thermomechanical loading; the effect, however, is not significant at small degrees of out-of-phase loading, as shown previously by the authors for $\overline{\Delta T}_h = 0$ [16]. In addition, strain hardening [28, 29], in principle, will reduce the reverse plasticity regime compared to the perfectly plastic material behaviour assumed here. Lastly, it should be also mentioned that isotropic elasticity and plasticity were assumed here; in single crystal Ni-blades, the thermal stresses acting along the blade chord direction (direction- θ of Fig 9a in the current context) will form random angles with the principal crystal orientations and as a result they will generally increase stresses compared to the isotropic case [35, 36]; crystal slip will also alter the material plastic behaviour and potentially also the ratchetting resistance of the structure.

The present study provides a foundation for understanding 3D effects. The analysis of Section 4 can be extended to account for stresses and strains in two directions (Fig 1b), as well as hole effects [32, 37]. It also provides a useful reference for developing direct numerical methods for ratchet boundary determination [38] and, generally, structural integrity assessment [24].

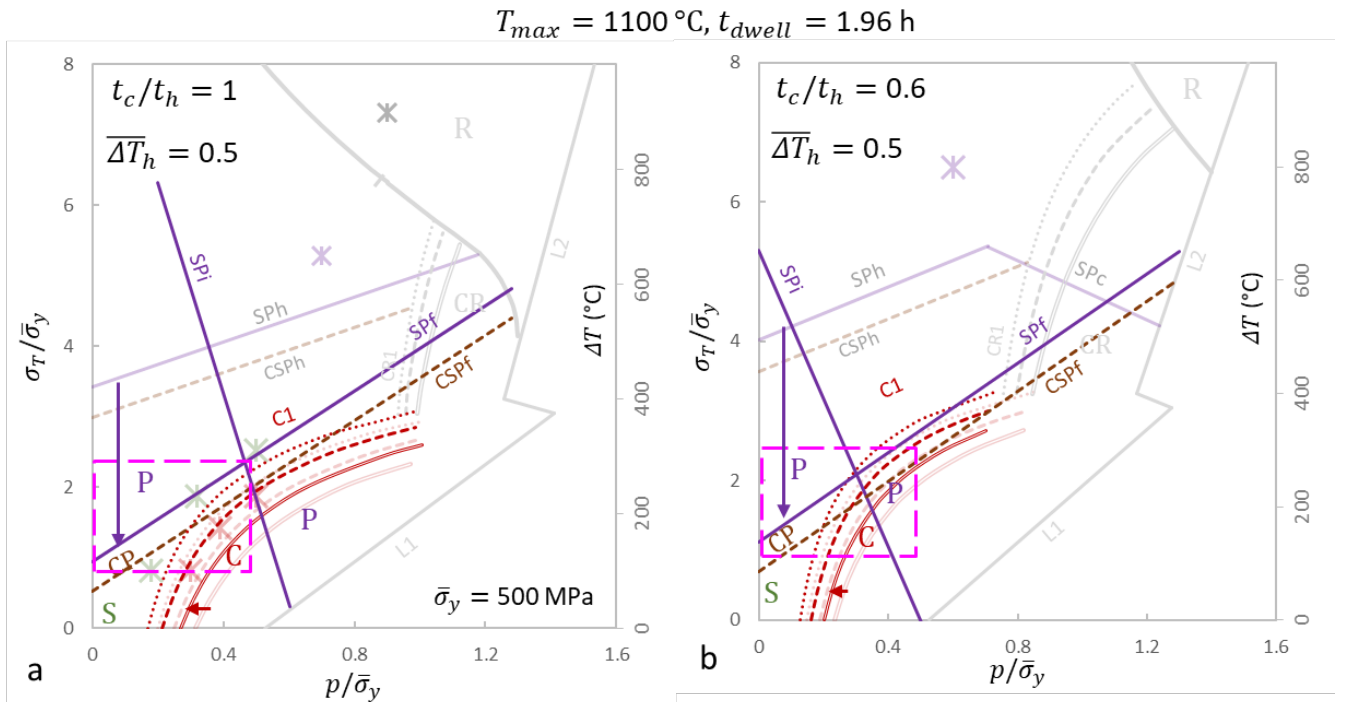


Figure 10. Interaction diagrams for the 3D geometry of Fig 9a showing the local reverse plasticity regimes (P) at the film and impingement holes due to the local stress concentration as well as the shift of the creep curves C1 to lower p values due to the net wall section reduction by the holes. SPf and SPi are the shakedown-reverse plasticity boundaries for the film and impingement holes, respectively. The boundaries in the background correspond to the 2D analytical predictions of Figs 7c-d. The mechanical and thermal loads, p and σ_T ($\sigma_T = E\alpha\Delta T$) are normalised by an average yield stress, $\bar{\sigma}_y = 500 \text{ MPa}$ and the pink box indicates the practical loading range for turbine blades. Fig 8a corresponds to wall thickness ratio, $t_c/t_h = 1$, whereas Fig 8b to $t_c/t_h = 0.6$.

7. Conclusions

Boundaries between global/structural ratchetting, global creep and reversed plasticity regimes have been derived analytically for double wall systems under in-phase thermomechanical loading and plane stress conditions. We show that the analytical route is a powerful, inexpensive strategy for: a) capturing the full landscape of behaviour; b) describing how regimes in which different mechanisms operate change with key geometric, temperature field and material model parameters; and c) provide a framework and background for performing targeted computational studies.

An extended Bree type analysis based on equilibrium and kinematic relations is found to provide the desired limit at which the structural response changes from local cyclic plasticity (leading to fatigue failure) into global ratchetting, whereas the boundary between classical elastic shakedown and ratchetting is determined by Koiter's shakedown theorem and equilibrium considerations. Certain types of mechanisms are triggered by the thermal gradient through the hot wall and involve plasticity at the extremes of the loading cycle, displaying a relevance with Bree type mechanisms for in-phase loading [30]. Other types of behaviour are induced by the thermal membrane stresses related to the coupling of the behaviour of the two walls. This gives rise to a rich range of different types of behaviour, including effects generated by the temperature dependence of the plastic and creep properties that involve plastic deformation at instances during the cycle other than at the extremes of the cycle.

The number of active ratchet mechanisms reduces when the yield stress decreases with temperature, because cyclic plasticity in the location of maximum temperature dominates over ratchetting. This effect is enhanced when the temperature difference between the walls decreases and the thermal gradient through the hot wall increases. Compressive ratchetting, enhanced by creep, at zero mechanical load is found to be a possibility, but this occurs in the extreme situation when the temperature field only involves a thermal difference between the walls.

In the practical loading range the system will suffer from local cyclic plasticity at the outer rim of the film hole and simultaneous global creep deformation. The higher the centrifugal loading and/or the lower the inner wall thickness, the more severe the creep deformation and the less severe the local fatigue at the film hole. Low inner wall thicknesses, however, can lead to prohibitive creep rates as well as cyclic plasticity at the impingement hole. These results highlight the trade-off between fatigue at the film and impingement holes as well as between fatigue at the film hole and global creep deformation. This showcases the need for evaluating the details of cyclic plastic deformation at holes in order to determine the optimal wall thickness ratio in terms of overall mechanical performance and cooling effectiveness.

The analytical methodology and Bree type interaction diagrams are relevant to a wide range of multi wall systems and form the basis for studying the mechanical performance of more complex 3D geometries.

Appendix A. Derivation of SR1 and SR1' boundaries for material model B

For material model B, the SR1(i-ii) equations in Section 4.1.1 become:

$$\int_{-\left(\frac{t_h}{2}-a\right)}^0 \left(\sigma_{y_h}(y = -a, \tau_1) + \xi \sigma_T^s \frac{\overline{\Delta T}_h}{t_h} \right) d\xi + \int_{-a}^{y_{tr}} \sigma_{y_h}(y, \tau_1) dy + \sigma_{y_0} \left(\frac{t_h}{2} - y_{tr} \right) + \sigma_{y_0} t_c = p^s(t_c + t_h) \quad (i)$$

(SR1)

$$\int_{-a}^{t_h/2} \hat{\sigma}_h^s(y, \tau_1) dy + \hat{\sigma}_c^s(\tau_1) t_c = \sigma_{y_0} \left(\frac{t_h}{2} - a \right) + \int_{-a}^{y_{tr}} \sigma_{y_h}(y, \tau_1) dy + \sigma_{y_0} \left(\frac{t_h}{2} - y_{tr} \right) + \sigma_{y_0} t_c \quad (ii)$$

where $y_{tr} = t_h(T_{max} - T_{tr})/(\overline{\Delta T}_h \Delta T) - t_h/2$ is the position in the hot wall below which the inner fibres of the hot wall yield in the cold yield strength regime at full load. This condition occurs at large $\overline{\Delta T}_h$ ($T_{max} = 1100$ °C) and gives the SR1 boundaries in Figs 7e-f. As $\overline{\Delta T}_h$ decreases the condition $y_{tr} = t_h/2$ prevails, such that the entire hot wall yields in the hot yield strength regime. This is the case in Figs 7a-d, and the corresponding SR1 boundaries are found by using $y_{tr} = t_h/2$ in the above equations.

Appendix B. Derivation of PR1 boundary for material model B

For material model B, the PR1 (i-iv) equations in Section 4.1.2 become:

$$- \int_{-\frac{t_h}{2}}^{-b} \sigma_{y_h}(y, \tau_1) dy + \int_0^{a+b} \left(-\sigma_{y_h}(y = -b, \tau_1) + \xi \sigma_T^s \frac{\overline{\Delta T}_h}{t_h} \right) d\xi + \sigma_{y_0} \left(\frac{t_h}{2} - a \right) + \sigma_{y_0} t_c = p^s(t_c + t_h) \quad (i)$$

$$\sigma_{y_0} \left(\frac{t_h}{2} + a \right) + \int_0^{\frac{t_h}{2}-a} \left(\sigma_{y_0} - \xi \sigma_T^s \frac{\overline{\Delta T}_h}{t_h} \right) dy + \sigma_c(\tau_0) t_c = 0 \quad (ii)$$

(PR1)

$$\frac{\sigma_{y_0}}{E} + \alpha T_h(y = a) = \frac{\sigma_{y_0}}{E} + \alpha T_{min} + \varepsilon_{p_c}(\tau_1) \quad (iii)$$

$$\frac{\sigma_{y_0}}{E} = \frac{\sigma_c(\tau_0)}{E} + \varepsilon_{p_c}(\tau_1) \quad (iv)$$

and the relation $\sigma_T^s \overline{\Delta T}_h / t_h = 2\sigma_y / (a + b)$ becomes $\sigma_T^s \overline{\Delta T}_h / t_h = [\sigma_{y_h}(y = -b, \tau_1) + \sigma_{y_0}] / (a + b)$. The above hold when the inner fibres of the hot wall ($y > a$) are in the cold yield strength regime, i.e. the transition position, y_{tr} , lies within the elastic core in Fig 3b. This is the case in Figs 7e-f due to $\overline{\Delta T}_h = 1$; when $\overline{\Delta T}_h = 0.5$ (Fig 7c) the above equations are modified to include the inner fibres of the hot wall in the hot yield strength regime.

Appendix C. Derivation of PR2 boundary for material model B

For material model B, the PR2 (i-iv) equations in Section 4.1.3 become:

$$-\int_{-\frac{t_h}{2}}^a \sigma_{y_h}(y, \tau_1) dy + \int_0^{\frac{t_h}{2}-a} \left(-\sigma_{y_h}(y = a, \tau_1) + \xi \sigma_T^s \frac{\overline{\Delta T_h}}{t_h} \right) d\xi + \sigma_{y_0} t_c = p^s(t_c + t_h) \quad (i)$$

$$\sigma_{y_0} t_h + \sigma_c(\tau_0) t_c = 0 \quad (ii)$$

(PR2)

$$-\frac{\sigma_{y_h}(y = a, \tau_1)}{E} + \alpha T_h(y = a, \tau_1) = \frac{\sigma_{y_0}}{E} + \alpha T_{min} + \varepsilon_{p_c}(\tau_1) \quad (iii)$$

$$\frac{\sigma_{y_0}}{E} = \frac{\sigma_c(\tau_0)}{E} + \varepsilon_{p_c}(\tau_1) \quad (iv)$$

Appendix D. Derivation of length b_0 for mechanism group PR4

During loading, the lengths a , b , which define the elastic-plastic interfaces (Fig 3f), decrease from their initial value, $t_h/2$ (no plasticity), down to the characteristic values, a_i , b_i (white dashed lines in Fig 3f). As the load increases further, the two elastic plastic interfaces then translate towards the outer fibres of the hot wall to satisfy equilibrium with the load p^s , i.e. the length, a , decreasing below a_i , whereas b increases back to its initial value. This implies that b_0 is the minimum value of b during loading, which defines the actual region where plastic strain does not occur until full load (between $y = -b_i$ and $y = a$ in Fig 3f) and the region where stresses are within yield at full load but plastic strain has occurred during loading (between $y = -b$ and $y = -b_i$ in Fig 3f). This phenomenon occurs only when the hot wall experiences tensile and compressive yielding during loading (PR1 and PR4 only) and is significant in the double wall system because tensile yielding of the cool wall during loading promotes stress redistribution in the hot wall. To determine b_i , it is necessary to determine the characteristic instance, τ_i , and the corresponding load/temperature scaling factor, k_i , when the condition $b = b_i$ occurs, as follows. At an instance, τ , during loading, with corresponding load/temperature scaling factor, k equilibrium in Fig 3f (for model A) gives:

$$-\sigma_y \left(\frac{t_h}{2} - b \right) + \int_0^{a+b} \left(-\sigma_y + \xi k \sigma_T^s \frac{\overline{\Delta T_h}}{t_h} \right) d\xi + \sigma_y \left(\frac{t_h}{2} - a \right) + \sigma_y t_c = k p^s(t_c + t_h) \quad (D1)$$

and the general relationship for the slope of the elastic stress reads:

$$k \sigma_T \overline{\Delta T_h} / t_h = \frac{2\sigma_y}{a + b} \quad (D2)$$

The above equations determine a function $b(\tau)$, which must satisfy $\partial b(\tau_i) / \partial \tau = 0$ when the maximum value $b = b_i$ occurs at the instance τ_i .

Appendix E. Derivation of PR7 boundary

Equilibrium at zero load in Fig 4f (for model B) gives:

$$\sigma_{y_0} t_h + \sigma_c(\tau_0) t_c = 0 \quad (i)$$

Postulating that at an instance $\tau_{k'}$, during re-loading the hot and cool walls respectively reach compressive and tensile yield gives:

$$\sigma_{y_0} + k' \hat{\sigma}_h = -\sigma_{y_h}(\tau_{k'}) \quad (ii) \quad (PR7)$$

$$\sigma_c(\tau_0) + k' \hat{\sigma}_c = \sigma_{y_0} \quad (iii)$$

where k' is the scaling factor corresponding to the unknown instance $\tau_{k'}$. Note that since $\overline{\Delta T}_h = 0$ the elastic solution $\hat{\sigma}_h$ for the hot wall given by Eq 4ii is uniform.

Appendix F. Calculation of stress relaxation $\Delta\sigma_{hcr}$ for the CSPh boundary

We assume that the outer fibre ($y = -t_h/2$) creeps according to:

$$Z \frac{\dot{\sigma}}{E} + \dot{\epsilon}_o \left(\frac{|\sigma|}{\sigma_o} \right)^n \text{sgn}(\sigma) \exp(x) = 0 \quad (F1)$$

where $x = -\frac{Q}{R} \left(\frac{1}{T_{max}} - \frac{1}{T_o} \right)$ and Z is the elastic follow-up factor that accounts for the influence of the surrounding fibres (which creep at a much lower rate) and of the cool wall (does not creep at all) on the stress relaxation of the outer fibre [2]. Since the local stress at the beginning of the creep dwell is limited by the compressive hot yield strength, i.e. $\sigma_h(y = -t_h/2, \tau_1) = -\sigma_{y_h}(y = -t_h/2, \tau_1)$, the stress at the end of a creep dwell, $\sigma_h(y = -t_h/2, \tau_{1'})$, (instance $\tau_{1'}$ in Fig 1d) can be obtained by integrating Eq F1 over t_{dwell} , to give:

$$\sigma_h(y = -t_h/2, \tau_{1'}) = \frac{-\sigma_{y_h}(y = -t_h/2, \tau_1)}{\left[1 + (n-1) \frac{E}{Z} \frac{\dot{\epsilon}_o}{\sigma_o^n} t_{dwell} \left| \sigma_{y_h}(y = -t_h/2, \tau_1) \right|^{n-1} \exp(x) \right]^{\frac{1}{n-1}}} \quad (F2)$$

which provides the magnitude of the stress relaxation, $\Delta\sigma_{hcr} = \sigma_h(y = -t_h/2, \tau_{1'}) - \sigma_h(y = -t_h/2, \tau_1)$, between the instances τ_1 and $\tau_{1'}$, in Fig 1d.

Based on the analytical calculation of $\Delta\sigma_{hcr}$ by the authors in for the case $\overline{\Delta T}_h = 0$ and the general approximate calculation here, it can be shown that $Z = 1 + t_h/t_c$ for $\overline{\Delta T}_h = 0$. As a result, a thick cool wall, i.e. $t_c \rightarrow \infty$, gives $Z \rightarrow 1$ and the outer fibre creeps under constant total strain, whereas a thin cool wall, i.e. $t_c \rightarrow 0$, gives $Z \rightarrow \infty$ and the outer fibre creeps under constant stress. Thus, $Z \rightarrow \infty$ and $Z = 1$ give the upper and lower bounds for the boundary CSPh. $t_c/t_h = 1$ in Fig 7a ($\overline{\Delta T}_h = 0$) gives $Z = 2$ and $t_c/t_h = 0.6$ in Fig 7b ($\overline{\Delta T}_h = 0$) gives $Z = 2.66$. For Figs 7c-d the factor Z can only be calibrated based on FE, as performed in . FE results presented here indicate that $Z = 1.6$ when $t_c/t_h = 1$ in Fig 7c ($\overline{\Delta T}_h = 0.5$) and $Z = 3.3$ when $t_c/t_h = 0.6$ in Fig 7d ($\overline{\Delta T}_h = 0.5$) and that $Z = 1.3$ when $t_c/t_h = 1$ in Fig 7e ($\overline{\Delta T}_h = 1$) and $Z = 1.7$ when $t_c/t_h = 0.6$ in Fig 7f ($\overline{\Delta T}_h = 1$).

Generally, the influence of Z on the CSPH boundaries in Figs 7a-f is found to be small, such that $Z = 1$ can be a reasonable (and conservative) assumption.

Acknowledgements

The work was supported by EPSRC programme grant EP/P000878/1.

References

1. Murray, A.V., P.T. Ireland, and A.J. Rawlinson. *An Integrated Conjugate Computational Approach for Evaluating the Aerothermal and Thermomechanical Performance of Double-Wall Effusion Cooled Systems*. in *ASME Turbo Expo 2017: Turbomachinery Technical Conference and Exposition*. 2017. American Society of Mechanical Engineers Digital Collection.
2. Skamniotis, C.G. and A.C. Cocks, *Creep-plasticity-fatigue calculations in the design of porous double layers for new transpiration cooling systems*. *International Journal of Fatigue*, 2021: p. 106304.
3. Skamniotis, C., M. Courtis, and A.C. Cocks, *Multiscale analysis of thermomechanical stresses in double wall transpiration cooling systems for gas turbine blades*. *International Journal of Mechanical Sciences*, 2021. **207**: p. 106657.
4. Reed, R.C., *The superalloys: fundamentals and applications*. 2008: Cambridge university press.
5. Murray, A.V., et al., *High Resolution Experimental and Computational Methods for Modelling Multiple Row Effusion Cooling Performance*. *International Journal of Turbomachinery, Propulsion and Power*, 2018. **3**(1): p. 4.
6. Murray, A.V., P.T. Ireland, and E. Romero, *Development of a Steady-State Experimental Facility for the Analysis of Double-Wall Effusion Cooling Geometries*. *Journal of Turbomachinery*, 2019. **141**(4).
7. Murray, A.V., P.T. Ireland, and E. Romero, *Experimental and Computational Methods for the Evaluation of Double-Wall, Effusion Cooling Systems*. *Journal of Turbomachinery*, 2020. **142**(11).
8. Courtis, M., et al., *Influence of Spanwise and Streamwise Film Hole Spacing on Adiabatic Film Effectiveness for Effusion-Cooled Gas Turbine Blades*. *International Journal of Turbomachinery, Propulsion and Power*, 2021. **6**(3): p. 37.
9. Ngetich, G.C., et al., *A Three-Dimensional Conjugate Approach for Analyzing a Double-Walled Effusion-Cooled Turbine Blade*. 2019. **141**(1): p. 011002.
10. Elmukashfi, E., et al., *Analysis of the Thermomechanical Stresses in Double-Wall Effusion Cooled Systems*. *Journal of Turbomachinery*, 2020. **142**(5).
11. Cerminara, A., R. Deiterding, and N.D. Sandham, *Transpiration cooling using porous material for hypersonic applications*. *Convective Heat Transfer in Porous Media*, 2019: p. 263.
12. Skamniotis, C.G. and A.C. Cocks, *2D and 3D thermoelastic phenomena in double wall transpiration cooling systems for gas turbine blades and hypersonic flight*. *Aerospace Science and Technology*, 2021: p. 106610.
13. Skamniotis, C.G. and A.C. Cocks, *Designing against severe stresses at compound cooling holes of double wall transpiration cooled engine components*. *Aerospace Science and Technology*, 2021: p. 106856.
14. Skamniotis, C. and A.C. Cocks, *Minimising stresses in double wall transpiration cooled components for high temperature applications*. *International Journal of Mechanical Sciences*, 2020. **189**: p. 105983.

15. Skamniotis, C. and A.C. Cocks, *Thermal and centrifugal stresses in curved double wall transpiration cooled components with temperature dependent thermoelastic properties*. International Journal of Solids and Structures, 2021: p. 111273.
16. Skamniotis, C. and A.C. Cocks, *Analytical shakedown, ratchetting and creep solutions for idealized twin-wall blade components subjected to cyclic thermal and centrifugal loading*. European Journal of Mechanics-A/Solids, 2022: p. 104652.
17. Bree, J., *Elastic-plastic behaviour of thin tubes subjected to internal pressure and intermittent high-heat fluxes with application to fast-nuclear-reactor fuel elements*. Journal of strain analysis, 1967. **2**(3): p. 226-238.
18. Ponter, A. and A. Cocks, *Thermal ratchetting of polycrystalline metals with inhomogeneous thermal properties*. Philosophical Magazine, 2013. **93**(22): p. 2947-2966.
19. Chaboche, J.-L., *Time-independent constitutive theories for cyclic plasticity*. International Journal of plasticity, 1986. **2**(2): p. 149-188.
20. Wan, V., et al., *Microstructure-sensitive fatigue crack nucleation in a polycrystalline Ni superalloy*. International Journal of Fatigue, 2016. **90**: p. 181-190.
21. Jiang, J., et al., *On the mechanistic basis of fatigue crack nucleation in Ni superalloy containing inclusions using high resolution electron backscatter diffraction*. Acta Materialia, 2015. **97**: p. 367-379.
22. Zhang, B., et al., *Constitutive modelling of ratcheting behaviour for nickel-based single crystal superalloy under thermomechanical fatigue loading considering microstructure evolution*. International Journal of Fatigue, 2020. **139**: p. 105786.
23. Zhang, B., et al., *Stress-controlled LCF experiments and ratcheting behaviour simulation of a nickel-based single crystal superalloy with [001] orientation*. Chinese Journal of Aeronautics, 2021. **34**(8): p. 112-121.
24. Ma, Z., et al., *A unified direct method for ratchet and fatigue analysis of structures subjected to arbitrary cyclic thermal-mechanical load histories*. International Journal of Mechanical Sciences, 2021. **194**: p. 106190.
25. Lytwyn, M., H. Chen, and A. Ponter, *A generalised method for ratchet analysis of structures undergoing arbitrary thermo-mechanical load histories*. International Journal for Numerical Methods in Engineering, 2015. **104**(2): p. 104-124.
26. Dye, D., et al. *Welding of Single Crystal Superalloy CMSX-4: Experiments and Modeling*. in *Superalloys 2004 (Tenth International Symposium)*. 2004.
27. Koiter, W.T., *General theorems for elastic plastic solids*. Progress of solid mechanics, 1960: p. 167-221.
28. Ponter, A. and S. Karadeniz, *An extended shakedown theory for structures that suffer cyclic thermal loading, Part 1: Theory*. 1985.
29. Ponter, A. and S. Karadeniz, *An extended shakedown theory for structures that suffer cyclic thermal loading, Part 2: applications*. 1985.
30. Bradford, R., *The Bree problem with primary load cycling in-phase with the secondary load*. International journal of pressure vessels and piping, 2012. **99**: p. 44-50.
31. Bradford, R., *The Bree problem with the primary load cycling out-of-phase with the secondary load*. International Journal of Pressure Vessels and Piping, 2017. **154**: p. 83-94.
32. Chen, H. and A.R. Ponter, *Linear Matching Method on the evaluation of plastic and creep behaviours for bodies subjected to cyclic thermal and mechanical loading*. International Journal for Numerical Methods in Engineering, 2006. **68**(1): p. 13-32.
33. Zheng, X. and F. Xuan, *Shakedown of thick cylinders with radial openings under thermomechanical loadings*. Journal of pressure vessel technology, 2012. **134**(1).
34. Reed, R.C., T. Tao, and N. Warnken, *Alloys-by-design: application to nickel-based single crystal superalloys*. Acta Materialia, 2009. **57**(19): p. 5898-5913.
35. Hou, N., et al., *The influence of crystal orientations on fatigue life of single crystal cooled turbine blade*. Materials Science and Engineering: A, 2008. **492**(1-2): p. 413-418.

36. Gao, H.-F., et al., *Probabilistic-based combined high and low cycle fatigue assessment for turbine blades using a substructure-based kriging surrogate model*. Aerospace Science and Technology, 2020: p. 105957.
37. Chen, H. and A.R. Ponter, *A simplified creep-reverse plasticity solution method for bodies subjected to cyclic loading*. European Journal of Mechanics-A/Solids, 2004. **23**(4): p. 561-577.
38. Spiliopoulos, K. and K. Panagiotou, *A residual stress decomposition based method for the shakedown analysis of structures*. Computer Methods in Applied Mechanics and Engineering, 2014. **276**: p. 410-430.